https://doi.org/10.5194/egusphere-2026-2655
Preprint. Discussion started: 20 May 2026

# Geometric in-flight calibration of MAJIS (JUICE) during early cruise phase and LEGA flyby

Benoît Seignovert[1], François Poulet[2], Yves Langevin[2], Emiliano D'Aversa[3], Nicolas Ligier[2], Cydalise Dumesnil[2], Magali Mesbout[2], Cédric Leyrat[4], Sophie Jacquinod[4], Stéphane Le Mouélic[5], Gabriel Tobie[5], Nicolas Mangold[5], Giuseppe Piccioni[3], Federico Tosi[3], Katrin Stephan[6], Pasquale Palumbo[3], Livio Agostini[3], Luca Penasa[7], Laetitia Le Deit[5], Thomas Cornet[8], Ines Belgacem[8], Marc Costa-Sitja[8], Alfredo Escalante Lopez[8], and Simeon Schmauß[5]

[1] Observatoire des Sciences de l'Univers Nantes Atlantique (Osuna/UARO), CNRS UAR-3281, Nantes Université, Nantes, France
[2] Institut d'Astrophysique Spatiale (IAS), Bures-sur-Yvette, France
[3] Istituto di Astrofisica e Planetologia Spaziali (INAF/IAPS), Rome, Italy
[4] Laboratoire d'Instrumentation et de Recherche en Astrophysique (LIRA), Paris, France
[5] Laboratoire de Planétologie et Géosciences (LPG), CNRS UMR 6112, Nantes Université, Nantes, France
[6] German Aerospace Center (DLR), Berlin, Germany
[7] Osservatorio Astronomico di Padova (INAF/OADP), Padova, Italy
[8] European Space Astronomy Centre (ESAC), Madrid, Spain

**Correspondence:** Benoît Seignovert (research@seignovert.fr)

**Abstract.** In August 2024, MAJIS, the visible and infrared mapping spectrometer onboard the ESA-Juice spacecraft, collected its first observations of resolved targets during Lunar and Earth Gravity Assist maneuver (LEGA). One month before, during payload checkout 2 (PC2), MAJIS performed two starfield observations to evaluate its post-launch geometric performances that can be compared with the LEGA data. This work presents an overview of the spatial distribution of the MAJIS signal collected at different scan angles and their position in MAJIS field of view. In PC2 starfields, 14 stars were identified, allowing us to derive a new in-flight alignment with an accuracy of 0.7 ± 0.4 MAJIS instantaneous field of view (IFOV). The offset between the nominal boresight of Juice remote sensing platform (+Z) and MAJIS boresight was evaluated to be 27 samples (along-slit) and 31 lines (cross-slit). With this new alignment, MAJIS observations on the Moon are co-aligned with JANUS camera with an accuracy of 2.2 ± 0.9 IFOV which could be improved to 1.1 ± 0.6 IFOV with bundle adjustment. A comparison of MAJIS Earth observations with simultaneous weather satellites observations confirmed that the MAJIS alignment is accurate for the full close Earth flyby. Residual misalignments with JANUS and NavCam remain visible in the Earth dataset but they can be easily corrected using small timing and scan angle adjustments (<10 IFOV). The instrument and frame kernels for MAJIS will be updated on the basis of these results. The improved co-alignment between MAJIS, JANUS and NavCam ensures strong synergy between the remote sensing instruments during the nominal scientific phase when they operate at the same time.

https://doi.org/10.5194/egusphere-2026-2655
Preprint. Discussion started: 20 May 2026

## 1 Introduction

The Juice (JUpiter ICy moons Explorer) spacecraft launched in 2023 (Grasset et al., 2013; Boutonnet et al., 2024) is the first ESA L-class mission and is on its way to explore the Jovian system. Onboard, among 11 instruments, the visible and infrared mapping spectrometer MAJIS (Moons And Jupiter Imaging Spectrometer) will collect hyperspectral cubes of Jupiter's atmosphere and its moons icy surfaces (Poulet et al., 2024b). Before the launch, an on-ground calibration campaign was performed to characterize the instrument spatial, spectral and radiometric performances (Vincendon et al., 2024; Filacchione et al., 2024; Haffoud et al., 2024; Langevin et al., 2024; Rodriguez et al., 2024; Stefani et al., 2025). After the launch, the Near Earth Commissioning Phase (NECP) and a few Payload Checkouts (PC) made it possible to assess the good behavior of the instrument in-flight (Poulet et al., 2024a). In August 2024, during the cruise phase, Juice performed a unique combined flyby of the Moon and the Earth during the first Lunar and Earth Gravity Assist (LEGA) providing opportunities for MAJIS to observe resolved targets (Dietz et al., 2026; Poulet et al., 2026). This opportunity was very valuable for MAJIS to improve its spectral and radiometric calibration (Langevin et al., 2026) as well as its geometric calibration (this work). Additional analyses were performed by the MAJIS science team, both on the Moon (Tosi et al., 2026; Zambon et al., 2026) and on the Earth (D'Aversa et al., 2026; Oliva et al., 2026; Guerlet et al., 2026). An overview of these Moon and Earth observations is presented in Poulet et al. (2026).

This work focuses on the in-flight geometric calibration of MAJIS for characterizing its boresight pointing with respect to the spacecraft reference frame and other remote sensing instruments. This task is particularly important because the on-ground determination of the MAJIS boresight alignment was conducted under significant planning development and schedule constraints, resulting in a final estimate based on a combination of measurements and modeling. Section 2 is dedicated to the description of MAJIS field of view (FOV) and its spatial extent. In section 3 we analyze the data collected during Payload Checkout 2 (PC2) on two starfields to perform a first in-flight geometric calibration and to derive a new orientation of the MAJIS reference frame. In section 4, these observations collected on the Moon and the Earth during LEGA are used for validating the new orientation of the MAJIS reference frame with respect to the spacecraft reference frame, and the cross-calibration of MAJIS with Juice high resolution camera JANUS (Jovis Amorum ac Natorum Undique Scrutator, Palumbo et al. (2025) and Tubiana et al. (2026)) and the navigation camera (NavCam, Gorog et al. (2019) and Cornet et al. (2026)) which were also operating during the LEGA flyby.

## 2 MAJIS field of view

MAJIS is a complex instrument and establishing a robust correspondence between the spatial distribution of the signal recorded by its detectors and the source direction in the observed scene is nontrivial. In this section, we first examine the detector pixel layout and we present the instantaneous field of view (IFOV) though the slit. Then we present the various windowing modes that can modify the extent of the FOV. Next, we detail how the step mirror mounted on the scan mechanism can be operated and its impact on the angular extent. Finally, we derive the total angular scanning extent accessible to MAJIS and outline the method used to reconstruct the spatial FOV geometry from all parameters.

https://doi.org/10.5194/egusphere-2026-2655
Preprint. Discussion started: 20 May 2026

### 2.1 Optical path

MAJIS is a visible and infrared imaging spectrometer composed of a single reflective optic collecting light coming from the spacecraft +Z axis direction. The first element on the optical path is a flat rotating mirror which controls the line of sight (LOS) of the instrument during the acquisition in the cross-slit direction, nearly parallel to spacecraft Y axis. The collected light is focused onto an internal slit which can be obturated by a shutter. A collimator then directs the beam onto a dichroic which separates it into visible and infrared channels. The beams are then spectrally dispersed by two gratings and imaged onto two focal plane arrays (FPA), one for the visible and near infrared channel (VISNIR) ranging from 0.50 to 2.35 $\mu$m, and another one for the infrared channel (IR) ranging from 2.25 to 5.56 $\mu$m (Poulet et al., 2024b).

A schematic representation of the instrument optical path is provided in Figure 1 showing the relationship between MAJIS optical subsystems and the relevant SPICE reference frames (Acton, 1996; Acton et al., 2018), which can be defined with a fixed rotation matrix with respect to the spacecraft frame (Figure 2). The orientation of the MAJIS LOS as a function of the scan angle is time variable and tracked with a SPICE C-kernel (CK) in the Juice kernels dataset (ESA SPICE Service, 2019) and in the MAJIS cube metadata.

### 2.2 Pixels layout

Each of the two MAJIS detectors (H1RG from Teledyne) is a 1024×1024 array of 18×18 $\mu$m pixels (Figure 3). Four lines and four columns along the edges of the frame (*reference pixels*) are not connected to the underlying diodes, so that only 1016×1016 pixels are collecting photons. The nominal spatial and spectral MAJIS resolution is obtained by averaging 2×2 pixels (see Langevin et al. (2022) and Royer et al. (2025) for details about the different detector readout strategies). In this work, we will use the term *pixel* for the physical units on the detector (18 $\mu$m), and the term *spaxel* for the averaged 2×2 pixels in nominal mode (36 $\mu$m). Thus, MAJIS has two sensitive areas of 508×508 nominal spaxels. The MAJIS slit, along the -X axis, is aligned with one of the detectors axes and each spaxel collects along the slit the spatial component (*samples*) and perpendicularly to the slit the spectral component (*spectels*).

The length of the slit was measured at 14.4 mm (Filacchione et al., 2024). This leads to a maximum of 400 samples (ie. 800 pixels) illuminated on the detector. This means that only these 400 samples, out of the 508 available in the active area could be illuminated. Therefore, MAJIS observations are limited to 400 samples.

At this stage, we assume that both detectors are co-aligned and only the location of the slit center is different between the VISNIR and the IR channels. On-ground and in-flight calibration with the internal calibration unit lamp (ICU) show that the slit center is located at pixel 500 and 488 respectively and is not centered on the detectors pixel grid (Filacchione et al., 2024). Most of the time, the first set of pixels to be readout (start pixel) can be adjusted by command for each detector independently to compensate this offset and to ensure that the recorded samples correspond to the same part of the slit.

Finally, it should be mentioned that MAJIS can perform limited spectral oversampling over part of the spectral range based on a spectral table by averaging the pixels with a 2×1 pattern instead of the nominal 2×2 pixels readout. In these cases up to 640 spectels can be collected per detector but the spatial dimension will remain unchanged (Langevin et al., 2022). On the

https://doi.org/10.5194/egusphere-2026-2655
Preprint. Discussion started: 20 May 2026

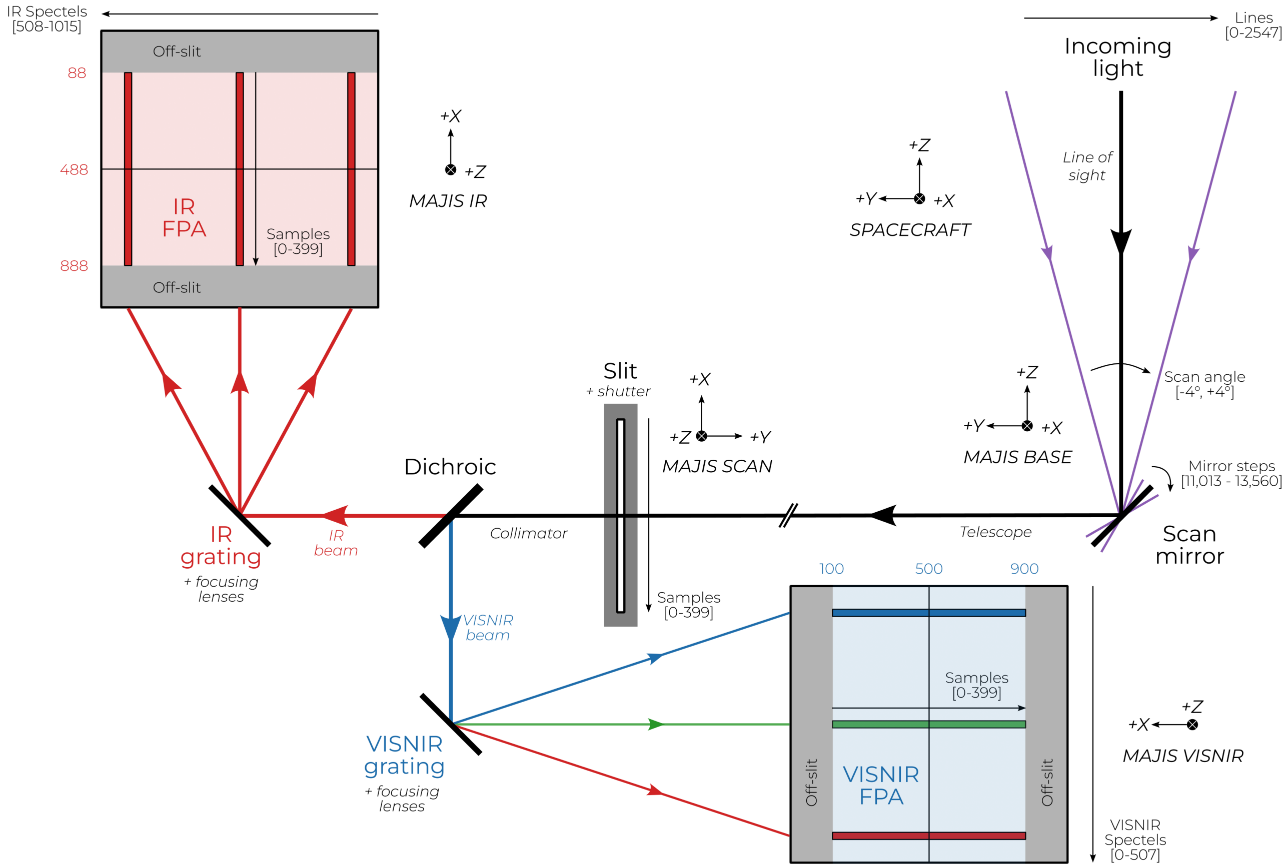

**Figure 1.** Schematic representation of MAJIS optical path. The SPICE reference frames (in uppercase) are represented with three perpendicular vectors (+X, +Y and +Z). The line of sight is along +Z, the scan mirror rotate around +X, the slit is perpendicular to +Z and is extended along -X (corresponding to the samples direction on the detectors). The dichroic splits the incoming beam in two beams (VISNIR and IR) which are both dispersed by a dedicated grating (corresponding to the spectels direction on the detectors) and focused on the two FPAs. Therefore, at each mirror position, the spectrally dispersed image of the slit is visible in both detectors. The rotation of the scan mirror only changes the scan angle of the slit line of sight. To keep this diagram in 2D, the optical path is artificially interrupted before the slit but in reality all these X, Y and Z vectors are co-aligned. A complete 3D representation can be found in Poulet et al. (2024b) in figures 8 and 10.

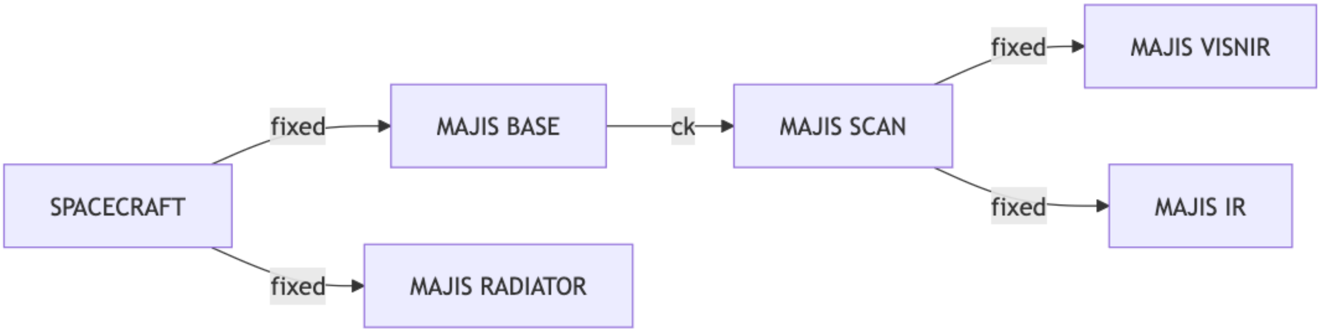

**Figure 2.** Schematic representation of the different SPICE reference frames hierarchy and their relationship. The rotation of the scan mirror is time variable and tracked with a CK. The other frames are related with a fixed offset frames.

other hand, it is possible to perform a spatial and spectral undersampling with a spaxel binning[1] by 2 or 4, in both directions independently. This binning is performed on top of the nominal 2×2 pixels readout (see Langevin et al. (2022) and Royer et al. (2025) for details). The corresponding binned area are also reported in Figure 3.

## 2.3 Instantaneous field of view

For each spaxel, the spatial extent along the slit ($x$) is defined by the individual spaxel size (36 $\mu$m), whereas the vertical extent, perpendicular to the slit ($y$), is constrained by the 36 $\mu$m slit width (Filacchione et al., 2024). Therefore, we can derive the spaxel instantaneous field of view (IFOV) in both directions as:

$$\mathrm{IFOV}_x = \arctan\left(\frac{2 \cdot p_x}{f}\right) \text{ and } \mathrm{IFOV}_y = \arctan\left(\frac{s_y}{f}\right) \tag{1}$$

where $f$ is MAJIS focal length (240 mm), $p_x$ the pixel size (18 $\mu$m), $s_y$ the slit width (36 $\mu$m). In nominal mode without any spatial binning, the spaxel instantaneous field of view is thus a square of 149×149 $\mu$rad. Thus, the full slit (400 samples) has an angular width of 3.4° (59.9 mrad).

If a spatial binning is applied, only the $\mathrm{IFOV}_x$ is increased by a factor 2 or 4. This means that the effective spatial footprint is no longer a square but a 1:2 or 1:4 rectangle (Figure 3). This non-square shape is usually combined with a longer integration time and/or multiple mirror steps to increase the spatial extent in the across slit direction ($\mathrm{IFOV}_y$) to match the $\mathrm{IFOV}_x$ dimension. If a spectral binning is applied, the IFOV is not modified.

---

[1] We use the term, binning here to distinguish the average 2×2 pixels nominal readout (= 1 spaxel) and the commanded binning between multiple spaxels. However, all these binning modes correspond to an average of multiple spaxels and not a sum of the spaxels, like a traditional binning mode would do. This distinction is important mainly for un-resolved target sources.

https://doi.org/10.5194/egusphere-2026-2655
Preprint. Discussion started: 20 May 2026

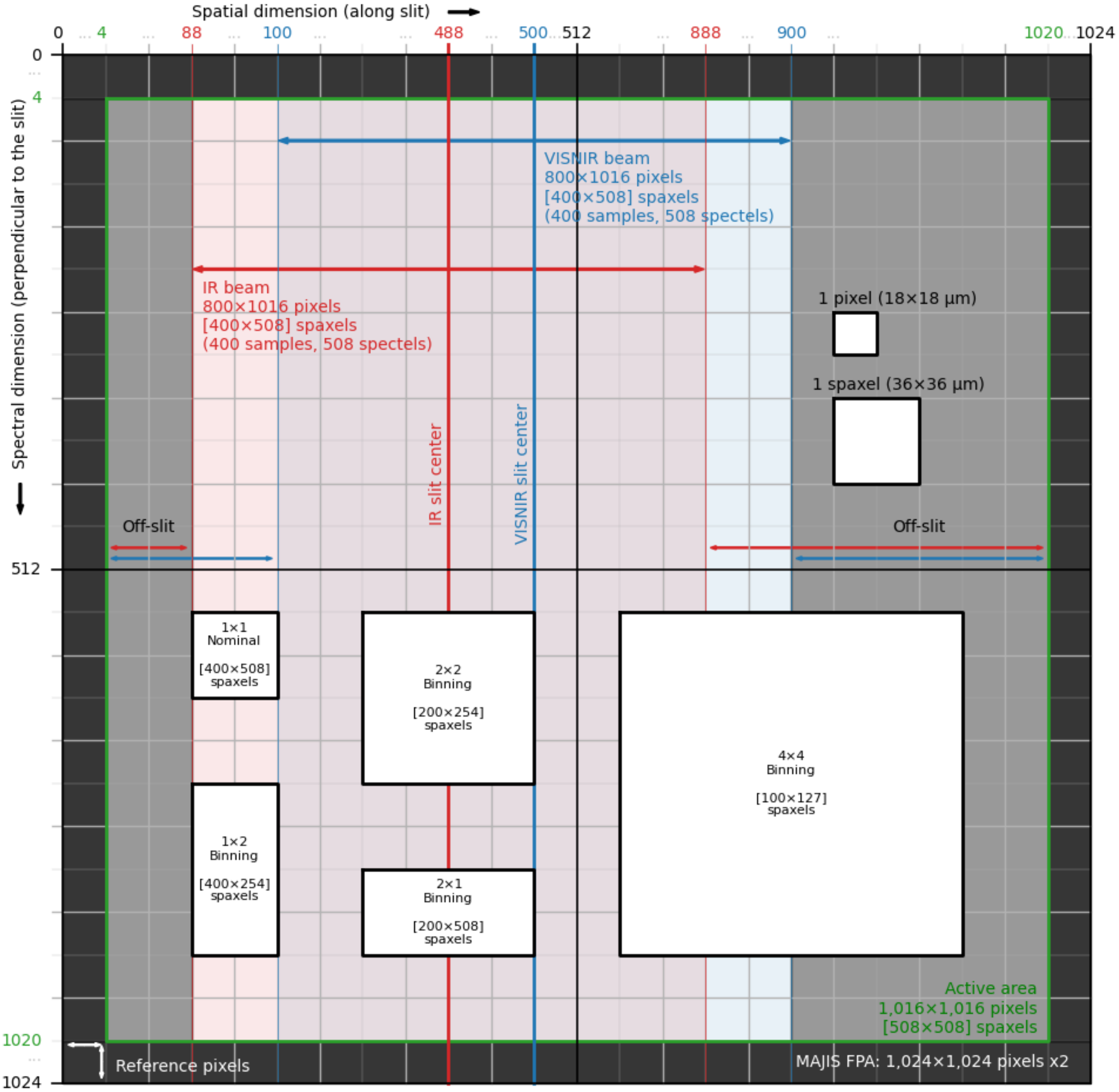

**Figure 3.** Pixel layout for MAJIS VISNIR and IR focal plane arrays (FPA). The top and left axis are labeled in pixels. The reference pixels are shown in black and the active sensitive area is contoured with a green line (1016×1016 pixels). The illuminated beams through the slit are represented in blue (VISNIR) and red (IR). The slit edges and center are located at a different positions for each channel (100, 500, 900 for the VISNIR and 88, 488, 888 for the IR). Off-slit areas are outside the illuminated part (in gray). In nominal mode, the pixels (18 $\mu$m) are averaged 2×2 to form a spaxel (36 $\mu$m) with a spatial extent along slit (sample) and a spectral extent perpendicular to the slit (spectel). Additional binning modes are illustrated in the bottom of the figure (assuming a nominal acquisition of 400 samples by 508 spectels).

https://doi.org/10.5194/egusphere-2026-2655
Preprint. Discussion started: 20 May 2026

### 2.4 Nominal acquisition and windowing modes

By default, MAJIS is designed to record its full slit length. In this case, the number of samples (NS) is set to 400 and the start pixel to 100 for the VISNIR channel and 88 for the IR channel (Figure 4). It is also possible to acquire only a subpart of the slit by limiting the number of samples read. This is particularly important when acquiring data on a very bright target (e.g. the Earth or the Moon) where only 64 pixels can be acquired during a 100 ms exposure (Poulet et al., 2026). This windowing method can also be very useful to limit MAJIS data volume for long distance observations, when the target covers only a very limited part of the slit. In this case, the number of pixels can be set as a multiple of 16 and can be combined with any start pixel value. For example, to acquire the left part of the slit (Figure 5), the start pixel is kept at 100 and 88 for the VISNIR and IR channels respectively but the number of pixels limited to NS = 64. Similarly, it is possible to center the windowing in the middle of the slit with a start pixel of 436 and 424 respectively and keeping the NS = 64 (Figure 6).

It is also possible to start the observation at a start pixel location outside the illuminated slit. In this case, the first samples acquired will be off-slit and should not record any light though the slit. This configuration is particularly interesting to assess the amount of stray light collected (Langevin et al., 2026). Figure 7 provides an example of a 64 samples acquisition on the left side of the slit where the first 15 samples are off-slit. It is also possible to perform the same off-slit acquisition on the right side of the slit.

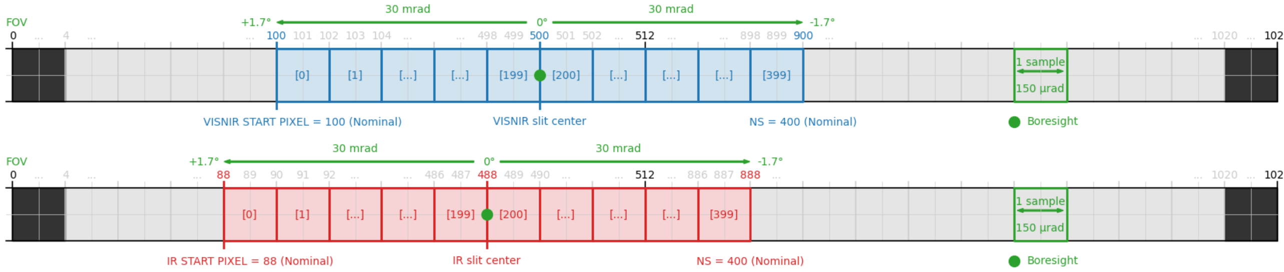

**Figure 4.** Full width detector nominal readout with no windowing (NS = 400) for the VISNIR channel (upper part, in blue) and the IR channel (lower part, in red). Here the start pixel is nominal (100 and 88 respectively). The black pixels on both ends represent the reference pixels, whereas the gray pixels are off-slit pixels (not illuminated). The green arrows at the top represents the angular extent with respect to the slit boresight.

When a spatial binning is applied, the width of the sample is increased by a factor 2 or 4. During PC2 starfields, only the full width of the slit was used (NS = 400). However, during LEGA, most of the observations were performed with a 64 or 128 samples window due to the short integration time constraints (see Poulet et al. (2026) and Table A1 in appendix).

### 2.5 First spatial dimension: slit samples

For each sample $i$ ranging from 0 to NS - 1, the sample center location can be expressed as a pixel offset $\Delta_x^c(i)$ with respect to MAJIS boresight:

https://doi.org/10.5194/egusphere-2026-2655
Preprint. Discussion started: 20 May 2026

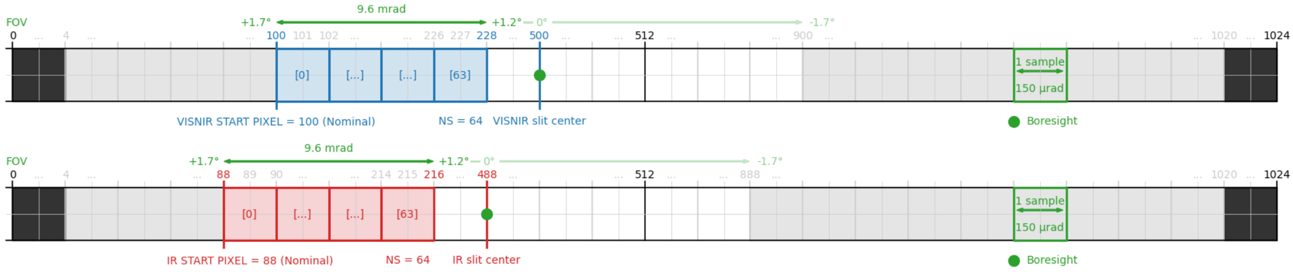

**Figure 5.** Same as Figure 4 but with a left windowing (here NS = 64). The white pixels are illuminated but not recorded.

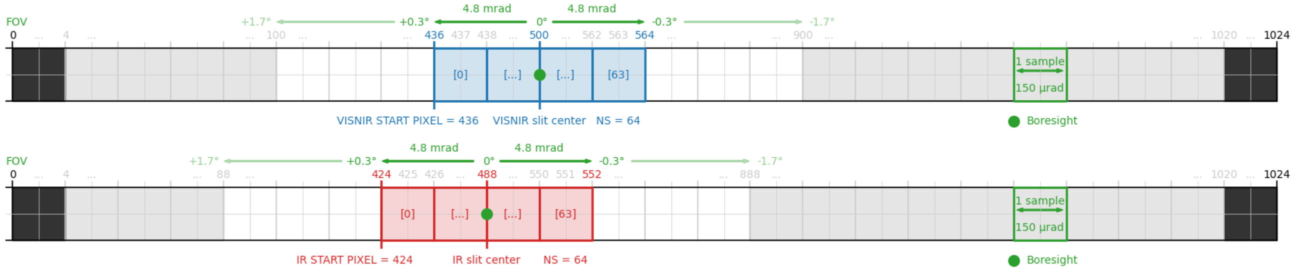

**Figure 6.** Same as Figure 5 but with a central windowing (NS = 64). Here the start pixels (436 and 424 respectively) are adjusted to be evenly distributed with respect to the slit center.

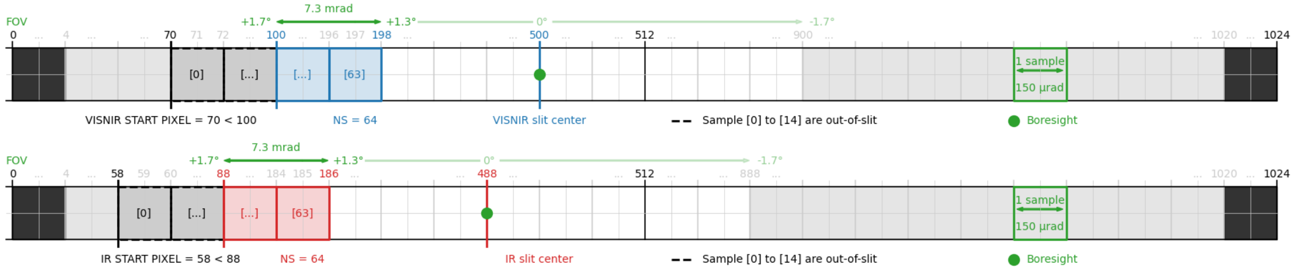

**Figure 7.** Same as Figure 5 but with a left off-slit windowing (NS = 64) whose readout starts before the illuminated area (with a start pixel 70 and 58 respectively). Here, the first 30 pixels (15 samples) are not directly exposed (in gray), only the remaining 98 pixels (49 samples) are.

$$\Delta_x^c(i) = x_c^\lambda - \left(x_0^\lambda + (2 \cdot i + 1) \cdot B_x\right) \tag{2}$$

with $x_0^\lambda$ the start pixel (e.g. 100 for the VISNIR channel, and 88 for IR channel), $x_c^\lambda$ the slit pixel center (500 for the VISNIR channel, and 488 for IR channel) and $B_x$ the spatial binning (1, 2 or 4). It should be noted that the minus sign here is coming from the fact that the +X axis in MAJIS reference frame is inverted compared with the sample readout. $x_c^\lambda$ was previously constrained in Filacchione et al. (2024) and should be the same for all observations, whereas NS, $x_0^\lambda$ and $B_x$ depend on the observation settings. At the moment, we consider that there are not enough in-flight data to constrain the tilt between the slit and the detectors axis, therefore, we assume that the potential offset $\Delta_c^y$ is always 0.

For the sample corners, the expression becomes:

$$\Delta_x^k(i) = x_c^\lambda - \left(x_0^\lambda + (2 \cdot i + x_k) \cdot B_x\right) \text{ and } \Delta_y^k(i) = y_k \tag{3}$$

with $(x_k, y_k) = (0, 0.5)$, $(2, 0.5)$, $(2, -0.5)$, $(0, -0.5)$ for the top-left, top-right, bottom-right, bottom-left corner respectively (with $k$ from 0 to 3).

Then, the samples centers and corners coordinates can be converted back to an angular offset with respect the boresight in the instrument reference frame:

$$\delta_x^{[c,k]}(i) = \arctan\left(\frac{p_x \cdot \Delta_x^{[c,k]}(i)}{f}\right) \text{ and } \delta_y^{[c,k]}(i) = \arctan\left(\frac{s_y \cdot \Delta_y^{[c,k]}(i)}{f}\right) \tag{4}$$

These angular extents are represented in green in Figure 4 to Figure 7.

### 2.6 Second spatial dimension: scan angle lines

To acquire its secondary spatial dimension (along Y in MAJIS reference frame), MAJIS can be operated in three different modes (Poulet et al., 2024b): (1) in a spacecraft stare using MAJIS internal scan mirror, (2) in a spacecraft slew with no mirror motion, (3) a combination of both, with a spacecraft slew and a mirror scan motion, e.g. for a fast flyby to perform motion compensation during a pushbroom phase. In all these cases, each line acquired will have a given mirror step position corresponding to a scan angle (Figure 1). The mirror rotation is discretized and commanded per observation. For each line recorded, its step position is reported into the cube metadata. MAJIS scan angle around X axis, is defined as the angular rotation of MAJIS boresight with respect to the line of sight. This angle ($\theta_y$) is linearly proportional to the commanded mirror step position ($m$):

$$\theta_y = 2 \cdot (a \cdot m + b) \tag{5}$$

https://doi.org/10.5194/egusphere-2026-2655
Preprint. Discussion started: 20 May 2026

with $a$ the mirror minimal increment ($\frac{360}{8192 \cdot 28}$ = 0.00156947°/step) and $b$ the mirror origin offset ($-(8192+4095)*a$ = -19.284145°). The factor 2 corresponds to the specular reflection of the beam on the scan mirror (Figure 1). It should be noted that when the mirror rotates with a positive increment, the scan angle around +X axis increases, but the motion of the boresight goes towards negative values along +Y axis. Thus, the lines direction increases towards -Y (Figure 1).

To avoid vignetting, the mirror step commanded for a MAJIS observation can only range between 11,013 and 13,560. This corresponds to a max scan angle of ±°4 with respect to the instrument line of sight. Each mirror step shifts the slit's boresight by 0.36 IFOV$_y$. When the full mirror extent is recorded with one step increments (e.g. in a starfield like PC2), the resulting cube will contain 2,548 lines. To optimize MAJIS coverage and limit the data volume, usually 3 mirror steps increment are used (equivalent to 1.09 IFOV$_y$).

For motion compensation or for a long exposure, it is also possible to request multiple mirror step positions per line. In these cases, it is required to compute the chronogram of the different positions during the integration time to reconstruct accurately the mean step position. This case did not occur in PC2, nor on LEGA and is not considered in this analysis.

### 2.7 MAJIS extended field of view

When we factor all the parameters described above, we can define a virtual MAJIS EXTENDED field of view, as the maximum angular field accessible to MAJIS. With a full slit and a complete angular scan, MAJIS FOV covers 3.4° along the X axis and 8° along the Y axis (Figure 8). Any part of this area can be covered with 1/3 oversampling (1 mirror step pitch) in the Y axis. Most of the time a pitch of 3 mirror steps is enough to cover the same FOV with minimal undersampling (<10%) but leading to a hyperspectral cube of only 849 lines rather than 2,548 lines. As we saw, slit windowing and spatial binning can be implemented to limit the active slit's extent and reduce the spatial resolution, proportionally decreasing the data volume produced.

All the information detailed in this section is reported in MAJIS frame (fk/juice_v46.tf) and instrument kernels (ik/juice_majis_v10.ti) which are made available in the Juice SPICE kernels dataset (ESA SPICE Service, 2019).

## 3 In-flight geometric characterization with starfields

### 3.1 PC2 acquisition geometry

Juice Payload Checkout 2 occurred in July 2024 (Table 1 and Dietz et al. (2026)). During this period MAJIS performed a series of calibration tests, mainly with its ICU. It was also able to perform its first star alignment in-flight. At that time, the thermal constraints on the spacecraft did not allow any pointing other than keeping -X axis aligned towards the Sun in order to use the high grain antenna has a heat shield. Only a roll around the spacecraft X axis was possible to point MAJIS boresight close to bright infrared stars. MAJIS observed 2 starfields on July 1st and 4th, 2024 in the Pisces constellation (Figure 9). The main stars targeted were $\delta$-Psc (HD 4656) and $\epsilon$-Psc (HD 6186), respectively, with G-magnitudes around 4 (Table 2). The spacecraft

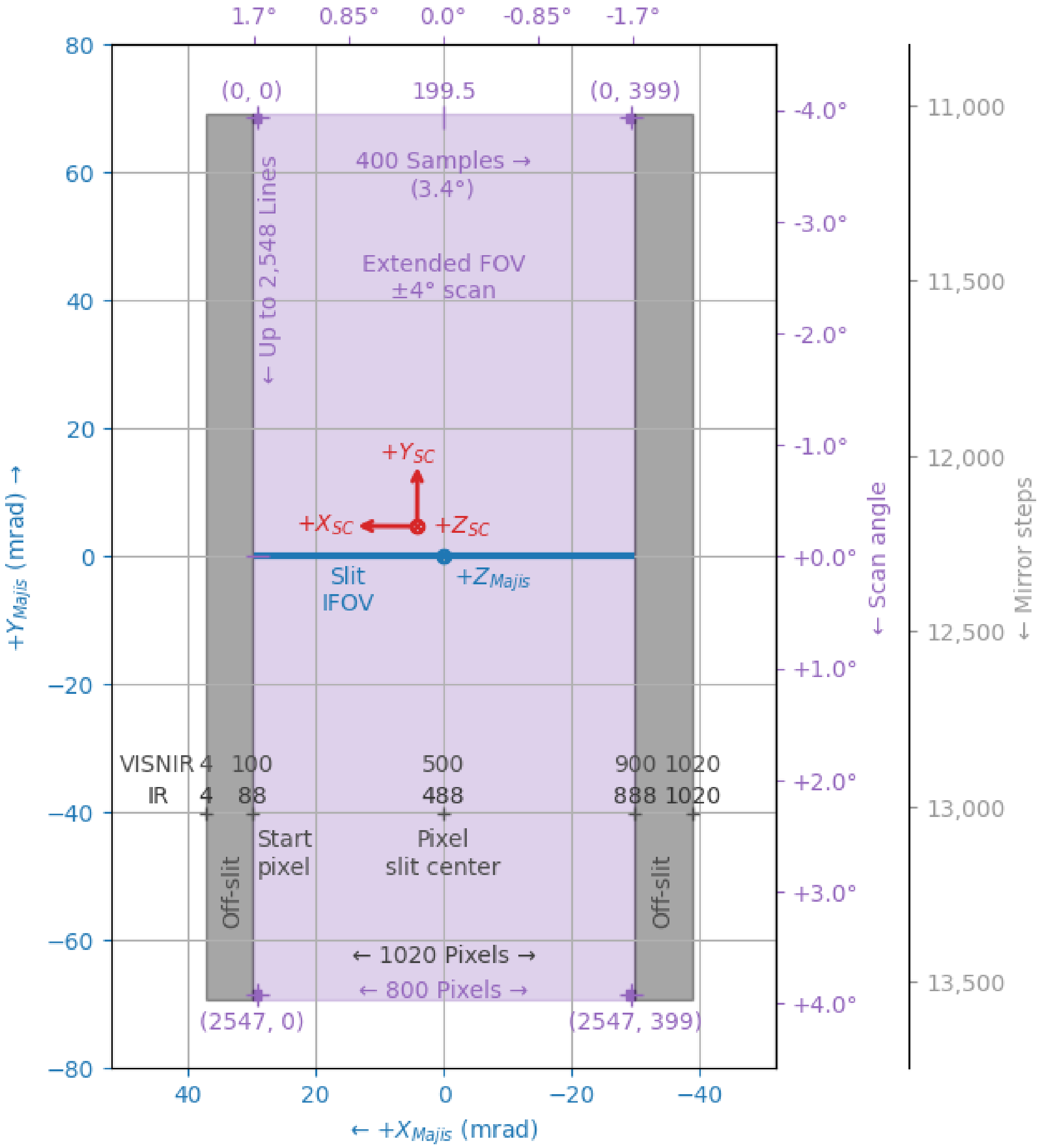

**Figure 8.** Angular extent of MAJIS FOV (purple area) for a scan angle ranging from -4° to +4° (up to 2,548 lines and up to 400 samples). The slit IFOV at a scan angle of 0° is shown in blue. Off-slit areas, which do not collect light though the slit, are indicated in gray on either side. Detector pixels coordinates along the slit are given in black. Image indices (line, sample) refer to the spaxel center (in purple). The relationships between the scan angle and the mirror steps are reported on the right part of the figure. The location and orientation of the spacecraft frame (after PC2 alignment) are shown in red.

https://doi.org/10.5194/egusphere-2026-2655
Preprint. Discussion started: 20 May 2026

**Table 1.** Cruise Payload Checkouts campaigns timeline.

| Cruise phase | Date | Comments |
|---|---|---|
| NECP | 2023-06 | No starfield |
| PC1 | 2024-01 | No starfield |
| PC2 | 2024-07 | 2 starfields |
| PC3 | 2025-03 | No starfield |
| PC4 | 2026-02 | 5 starfields |
| PC5 | 2026-07 | No starfield |

performed two inertial stares during 42 minutes and MAJIS used its internal mirror to scan the sky. In both cases, the scan angle ranged from -4° to +4° with 1 step mirror pitch (Figure 9).

### 3.2 Star centroid identification

Identifying the stars in MAJIS field of view is very challenging, especially when their signal is low. To extract the most accurate stars centroids from this dataset, we first queried the Gaia DR3 catalog (Gaia Collaboration et al., 2023) all the expected stars in MAJIS FOV with a magnitude lower than 8. The star locations $(\alpha^\star, \delta^\star)$ in the catalog are expressed in the International Celestial Reference System (ICRS) with their right ascension $(\alpha^{\mathrm{ICRS}})$ and declination $(\delta^{\mathrm{ICRS}})$ at J2016 epoch and are corrected for proper motion $(\mu)$ and spacecraft parallax $(p)$:

$$\alpha^\star = \alpha^{\mathrm{ICRS}} + \mu_\alpha \cdot \Delta t + p_\alpha^{\mathrm{SC}} \text{ and } \delta^\star = \delta^{\mathrm{ICRS}} + \mu_\delta \cdot \Delta t + p_\delta^{\mathrm{SC}} \tag{6}$$

where $\Delta t$ is the temporal offset between 2016 and the acquisition date.

Then, MAJIS VISNIR signal is extracted within a box of ±40 samples and lines around the expected star location. This signal is stacked on all the VISNIR wavelengths, the median is removed and only the part of the signal greater than 5 times the standard deviation in the box is retained. The data are oversampled by a factor 10 to get sub-pixel accuracy and we use SciPy *griddata* interpolation with a 2D cubic method (Virtanen et al., 2020). All the lines and all the samples are summed on each axis and the resulting histograms are used to identify the peak intensity for both axes. When the star is properly located, the procedure above is re-run with the new expected star location but this time with a ±10 samples and lines window to improve the centroid location down to a sub-spaxel accuracy. An example of this method on $\delta$-Psc star is presented in Figure 10. We can see that the star image has a nearly Gaussian shape which is centered around its maxima.

### 3.3 Stars alignment

Using the method above, 14 stars were identified in total from both starfields. The resulting stars centroids are reported in Table 2. Then, using the reconstructed SPICE kernels from *juice_ops_452_20241210_001* (ESA SPICE Service, 2019), we were

https://doi.org/10.5194/egusphere-2026-2655
Preprint. Discussion started: 20 May 2026

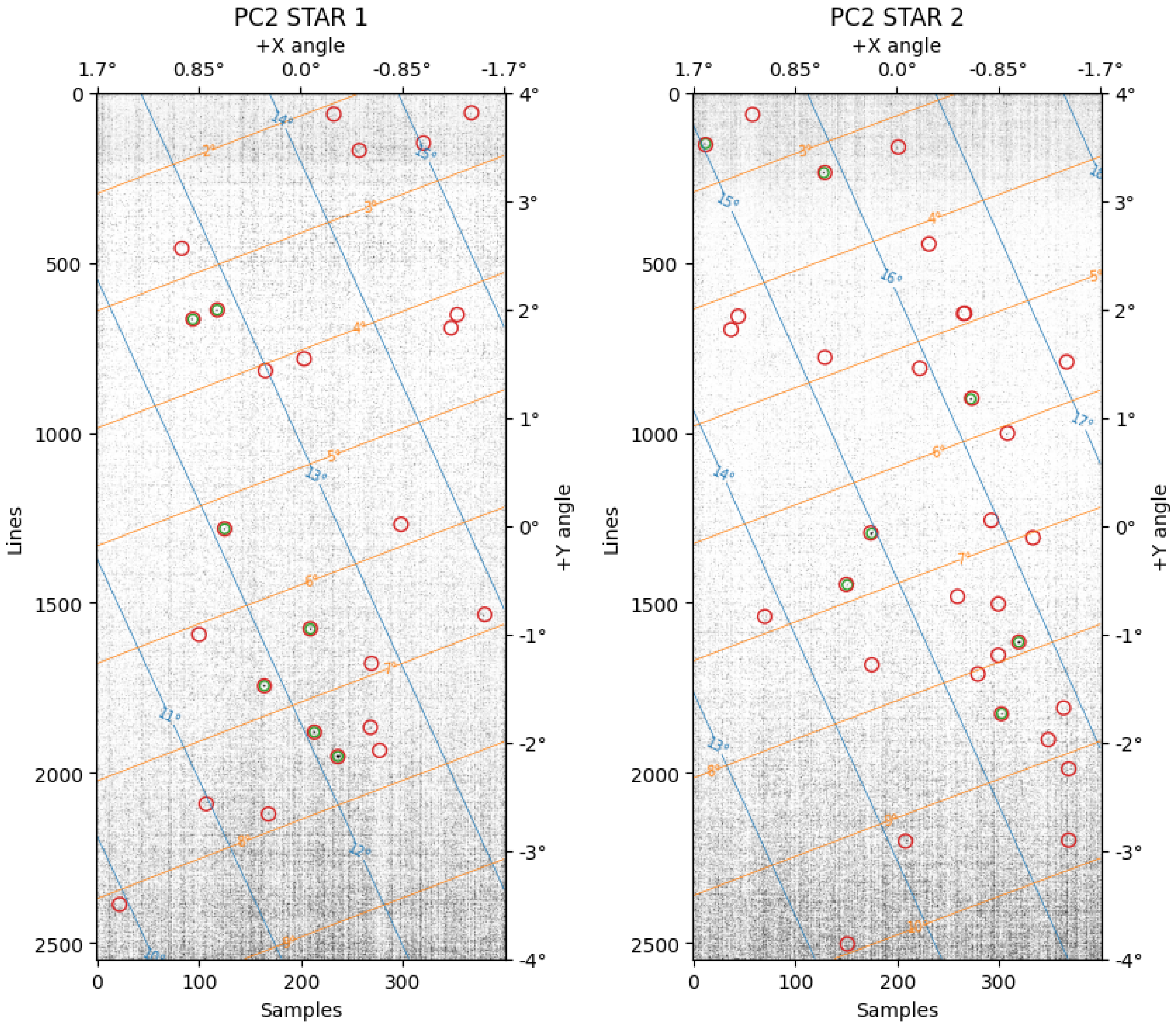

**Figure 9.** MAJIS starfields acquired during PC2 (left: July 1st, right: July 4th). The red circles correspond to the expected star locations based on the Gaia DR3 catalog. The green circles correspond to the stars detected by MAJIS and used in the star alignment. The blue and orange lines correspond to the RA and DEC coordinates on the sky. The top and right axes correspond to the angular offset with respect to MAJIS boresight.

https://doi.org/10.5194/egusphere-2026-2655
Preprint. Discussion started: 20 May 2026

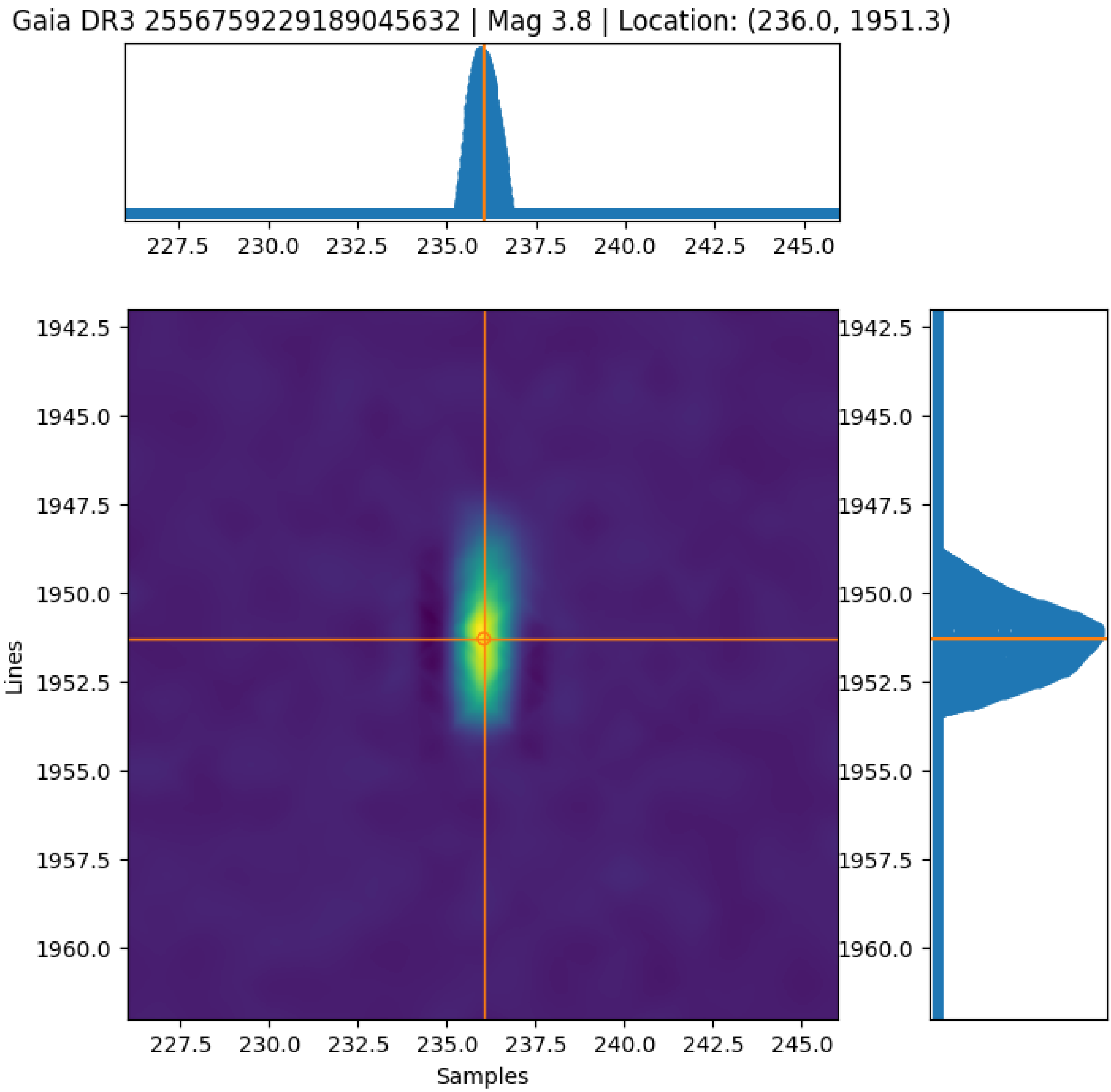

**Figure 10.** Example of star centroid identification on $\delta$-Psc star at sample 236.0 and line 1951.3 in the July 1st starfield.

**Table 2.** Stars centroids (samples and lines) observed with MAJIS during PC2 based from Gaia DR3 catalog and corrected from proper motion and parallax.

| Starfield | Name | Star ID | Gaia EDR3 | G magnitude | RA ($\alpha^\star$) | DEC ($\delta^\star$) | Sample | Line |
|---|---|---|---|---|---|---|---|---|
| PC2 STAR 1 | $\delta$-Psc | HD 4656 | 2556759229189045632 | 3.8 | 12.171161° | 7.584739° | 236.0 | 1951.3 |
| PC2 STAR 1 | | | 2552925644460225152 | 5.5 | 12.100862° | 5.272828° | 125.0 | 1282.1 |
| PC2 STAR 1 | | | 2556745141696841984 | 5.6 | 12.073302° | 7.299960° | 213.0 | 1879.9 |
| PC2 STAR 1 | | | 2556642955834891520 | 5.7 | 11.848536° | 6.740834° | 164.0 | 1743.5 |
| PC2 STAR 1 | | | 2550145254432544512 | 6.1 | 12.826506° | 3.384561° | 117.8 | 638.0 |
| PC2 STAR 1 | | | 2556428551067486720 | 7.0 | 12.416112° | 6.407141° | 209.1 | 1576.7 |
| PC2 STAR 1 | | | 2550156077749146752 | 7.5 | 12.602236° | 3.381208° | 93.9 | 665.9 |
| PC2 STAR 2 | $\epsilon$-Psc | HD 6186 | 2577673177300873216 | 4.0 | 15.735318° | 7.890306° | 319.0 | 1614.9 |
| PC2 STAR 2 | | | 2577273298665142528 | 5.2 | 14.957173° | 6.483192° | 174.8 | 1295.1 |
| PC2 STAR 2 | | | 2576354759779353088 | 5.5 | 16.219524° | 5.656163° | 272.0 | 890.0 |
| PC2 STAR 2 | | | 2577485916726441088 | 6.5 | 14.581258° | 6.844265° | 151.0 | 1446.7 |
| PC2 STAR 2 | | | 2580754558637186944 | 6.9 | 15.346157° | 8.450559° | 302.4 | 1825.2 |
| PC2 STAR 2 | | | 2539302386154060160 | 7.1 | 15.023375° | 2.632914° | 12.0 | 148.1 |
| PC2 STAR 2 | | | 2539771808899993344 | 7.2 | 15.858472° | 3.255466° | 129.0 | 234.3 |

able to estimate the offset between the expected and the observed star positions based on the ground calibration (Filacchione et al., 2024). On average the offset is about 0.056 ± 0.012° (977 ± 206 $\mu$rad), which correspond to 6.5 ± 1.4 IFOV.

Then we relaxed the constraint on the fixed rotation matrix between the SPACECRAFT and MAJIS BASE frames (i.e. TKFRAME_-28400_ANGLES) in order to minimized globally the distance between the expected star's location and the observed centroid for all the 14 stars. The best fit was obtained for a TKFRAME value equal to (0.235, 0.237, -0.272) ± (0.073, 0.003, 0.003). Here the uncertainties correspond to the square root of the diagonal terms of the covariant matrix. Therefore, the mean observed offset is significantly improved at 0.006 ± 0.003° (101 ± 54 $\mu$rad), which corresponds to 0.7 ± 0.4 IFOV (Figure 11).

At present, the dominant source of uncertainty arises from the first component of the TKFRAME corresponding to a rotation around the spacecraft +Z axis. This uncertainty may, for instance, reflect a residual misalignment between the mirror rotation axis and the slit. However, the limited number of stars detected so far prevents a more precise determination of this parameter.

### 3.4 Post-PC2 alignment with other instruments

As mentioned above, the updated TKFRAME values following the PC2 alignment have been incorporated into the MAJIS frame kernel (FK). This new alignment improves the characterization of the MAJIS boresight both relative to the spacecraft reference frame and other Juice remote sensing instruments. Figure 12 represents the different instrument boresights and FOVs in the spacecraft reference frame to illustrate their co-alignment. The offset between MAJIS boresight and the spacecraft +Z

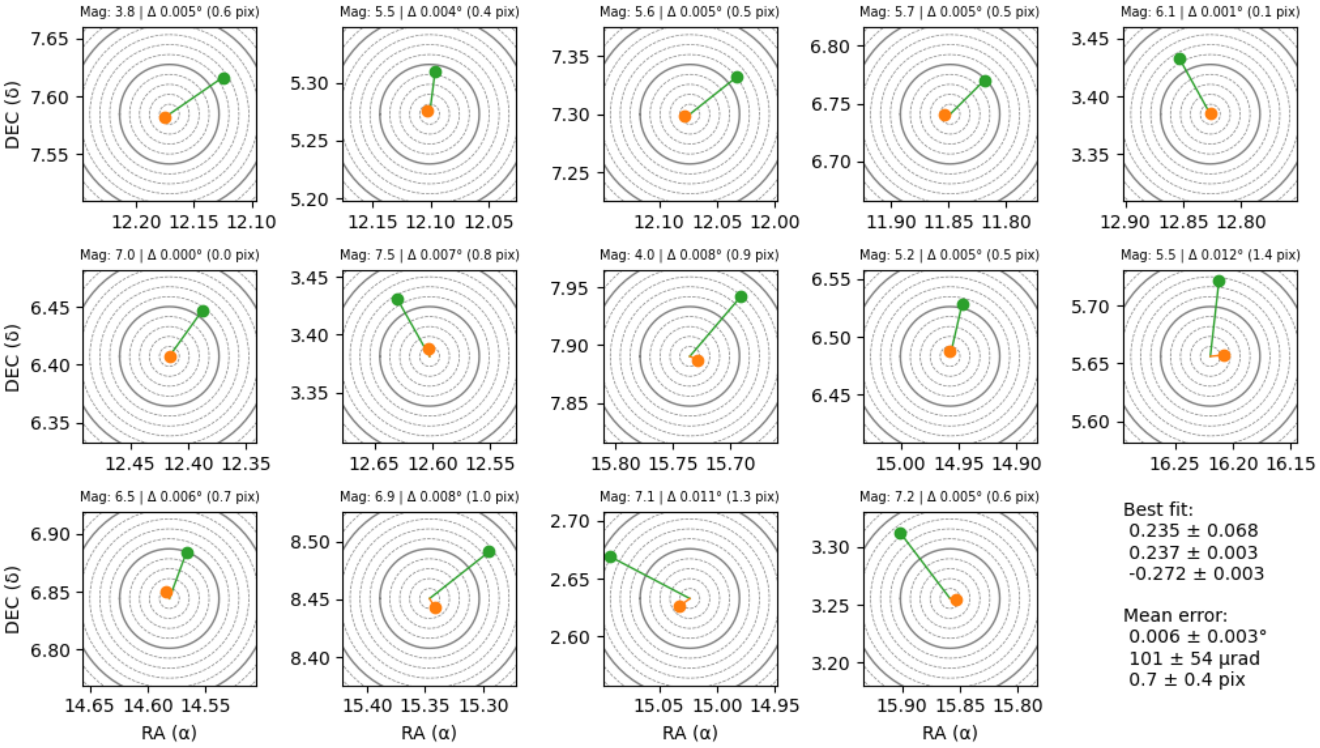

**Figure 11.** Stars alignment. In green, the star expected location based on ground calibration. In orange, the star's expected location after PC2 in-flight alignment. The best fit reported on the lower right corresponds to PC2 TKFRAME alignment. The gray dash circles correspond to 1 MAJIS IFOV increments (the solid lines correspond to 5 and 10 MAJIS IFOVs).

axis is measured at 0.238° along X and 0.271° along Y. This correspond to an offset of -27.7 samples and -31.5 lines in MAJIS extended field of view. The offsets between MAJIS boresight and the other instruments are reported in Table 3. These values are subject to changes, once the other instruments provide their own alignment corrections.

## 4 Analysis of the LEGA data

During Juice Lunar and Earth Gravity Assist (LEGA) in August 2024, MAJIS was able to operate during the Moon and the Earth flybys (Poulet et al., 2026). Even though the spacecraft was not allowed to rotate, the spacecraft +Z axis was pointed towards the Moon and the Earth to allow the instruments to perform their first calibration observation on resolved targets. The co-alignment between MAJIS, JANUS and NavCam allowed almost simultaneous observations (within a few minutes) over the same regions under identical illumination and viewing geometries (Poulet et al., 2026; Tubiana et al., 2026; Cornet et al., 2026).

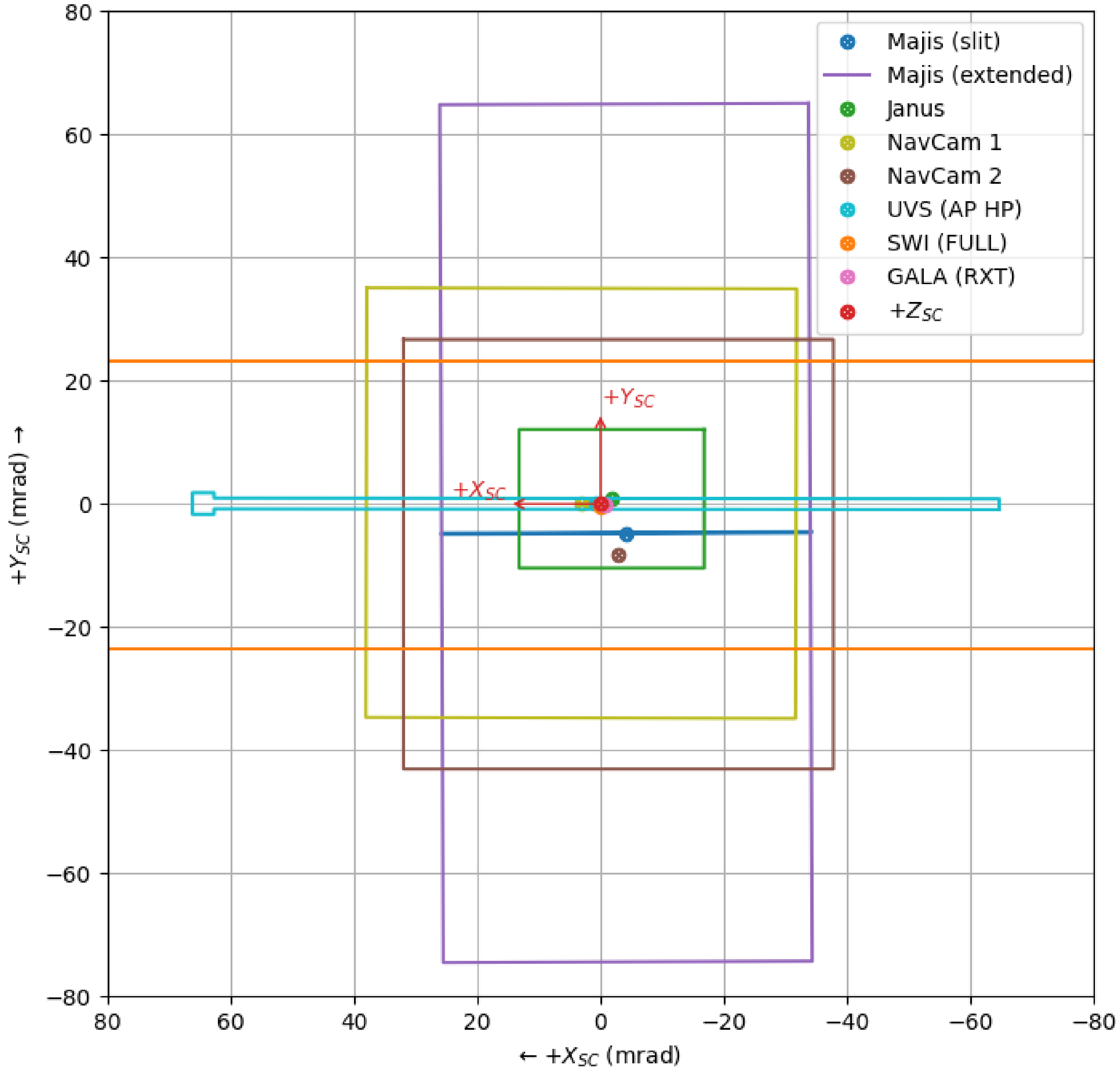

**Figure 12.** Pointing alignment post-PC2, where MAJIS FOV and boresight (in blue) are compared with other remote sensing instruments onboard Juice in the spacecraft reference frame.

**Table 3.** Relative angular offsets ($\delta$X and $\delta$Y) between MAJIS boresight and Juice remote sensing instruments. The offsets are also expressed as samples ($\Delta$S) and lines ($\Delta$L) offsets.

| Frame | $\delta$X | $\delta$Y | $\Delta$S | $\Delta$L |
|---|---|---|---|---|
| Spacecraft +Z | 0.238° | 0.271° | -27.7 | -31.5 |
| JANUS | 0.134° | 0.319° | -15.6 | -37.1 |
| NavCam-1 | 0.417° | 0.279° | -48.5 | -32.4 |
| NavCam-2 | 0.070° | -0.199° | -8.2 | 23.1 |
| UVS | 0.281° | 0.271° | -32.7 | -31.5 |
| SWI | 0.239° | 0.241° | -27.9 | -28.1 |
| GALA (RXT) | 0.187° | 0.262° | -21.8 | -30.5 |

## 4.1 Lunar gravity assist (LGA)

### 4.1.1 Acquisition geometry

On the Moon, 5 MAJIS observations were planned, one at the terminator with no scan around the boresight (full slit with 99 lines), then 2 surface observations using a significant part of the full scan extent (64 samples with 1,274 and 1,269 lines), one off-slit on the left (64 samples with 841 lines) and one observation at the limb (64 pixels with 535 lines with off-slit on the right). In this section we will only focus our analysis on the first 4 observations of the Moon surface (Poulet et al., 2026; Tosi et al., 2026; Zambon et al., 2026), listed below as LGA1 to LGA4 (Figure 13). JANUS observed the Moon surface continuously (Tubiana et al., 2026; Lucchetti et al., 2026), therefore, all the MAJIS observations overlap multiple JANUS observations when MAJIS scan angle is between -0.3° and +1.0°. For NavCam, only one image overlaps MAJIS FOV in a very small fraction of the NavCam field of view (Cornet et al., 2026).

### 4.1.2 Validation post-PC2 with JANUS

To retrieve MAJIS geometry on the Moon, we use the same reconstructed SPICE kernels dataset from *juice_ops_452_20241210_001*, as for PC2. In this case, however, we added three additional kernels (*moon_lola_dem_118m_v00.tf*, *moon_080317.tf* and *moon_pa_de421_1900-2050.bpc*) to ortho-rectify MAJIS observations using the lunar LOLA DEM (LOLA Science Team and Goddard Space Flight Center, 2014), with *MOON_ME* as our reference frame to ensure consistency with JANUS ortho-rectification pipeline. A visual comparison with the LRO LROC WAC global high-resolution mosaic at 100 m/pixel (LROC Team and Arizona State University, 2013) shows no discrepancies relative to the JANUS dataset. Therefore, we will use the JANUS mosaic acquired during the flyby under identical illumination conditions as our reference to measure MAJIS alignment offset (Figure 13).

For each MAJIS observation, we manually selected between 30 and 138 control points that correspond to recognizable features visible in both datasets. The mean haversine distance between the control points provides the offset between MAJIS

https://doi.org/10.5194/egusphere-2026-2655
Preprint. Discussion started: 20 May 2026

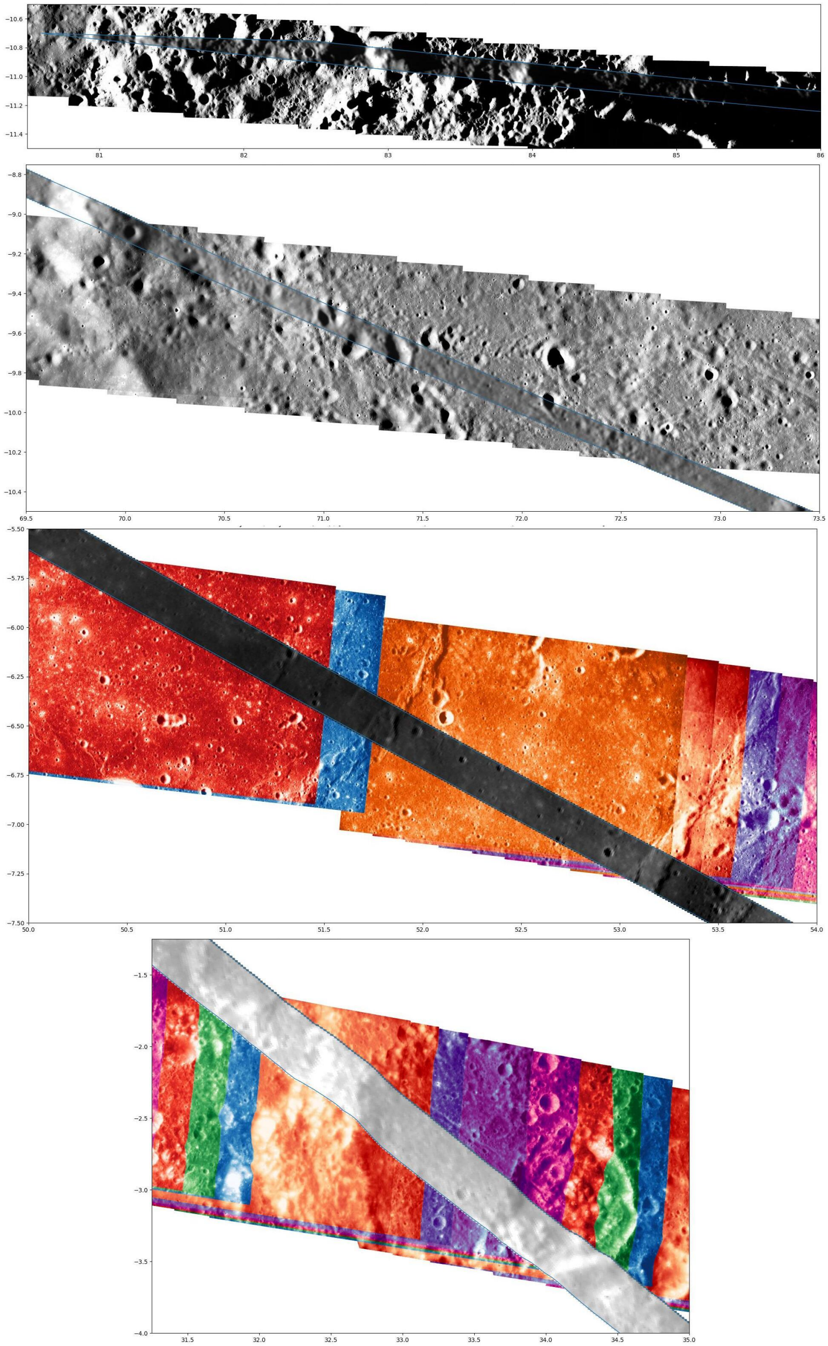

**Figure 13.** Overlays of MAJIS and JANUS observations on the Moon during LGA in August 2024 (LGA1 to LGA4 from top to bottom). The MAJIS image at 1.4 $\mu$m (in the foreground and contoured in blue) is superimposed on a JANUS mosaic in the background. JANUS images are colorized according to their acquisition filter. Both datasets share the same illumination and viewing geometry and were acquired nearly simultaneously. The alignment displayed here, after bundle adjustment, corresponds to an average offset of 1.1 ± 0.6 MAJIS IFOV.

**Table 4.** Number of control points and average offset before and after bundle adjustment (units are in MAJIS IFOV). The uncertainly corresponds to the standard deviation.

| Observation | Number of points | Offset before | Offset after |
|---|---|---|---|
| LGA1 | 138 | 2.2 ± 0.6 | 1.1 ± 0.6 |
| LGA2 | 30 | 1.3 ± 0.2 | 0.6 ± 0.3 |
| LGA3 | 60 | 1.5 ± 0.4 | 1.2 ± 0.5 |
| LGA4 | 33 | 4.0 ± 0.7 | 1.1 ± 0.6 |
| **Total** | **261** | **2.2 ± 0.9** | **1.1 ± 0.6** |

and JANUS and is expressed in units equivalent to the MAJIS IFOV. When using the star alignment derived from PC2 starfields, an averaged offset of 2.2 ± 0.9 MAJIS IFOV is found (Table 4, Figure 14). This value exceeds the uncertainty retrieved from the starfields (0.7 ± 0.4 MAJIS IFOV). This discrepancy may arise from multiple sources such as timing, image distortion or frame offset. Starfields are acquired in inertial pointing without any strict timing constraints, so a small mismatch during LGA between the commanded and the acquisition times is possible. A timing error would mostly project along the spacecraft slew direction. Since JANUS is overlapped by MAJIS around it's boresight MAJIS distortion is expected to be negligible in these cases. Finally, a frame offset would produce a more systematic shift. Therefore, to address this residual offset, we apply a global bundle adjustment to all the control points to evaluate this residual offset.

### 4.1.3 Bundle adjustment

The positions of all 261 control points (Table 4) are used simultaneously to retrieve a new TKFRAME value. We use the *curve_fit* method from SciPy (Virtanen et al., 2020) to minimize the distance between between MAJIS and JANUS control points. The resulting value (0.277, 0.216, -0.270) is compatible with the starfields measurements. The residual offset between MAJIS and JANUS is decreased down to 1.1 ± 0.6 MAJIS IFOV (Figure 14) and is compatible with PC2 uncertainties. This bundle adjustment is used as a diagnostic validation and not as a calibration update. This new TKFRAME value, it will not be reported in the instrument frame kernel because the presence of timing-related biases in LGA dataset has not yet been assessed.

It should be noted that the results from this bundle adjustment were also used to collocate JANUS pixels within the MAJIS spaxels in order to perform a cross-instrument radiance comparison (see figure 16 in Langevin et al. (2026) and Agostini et al. (2026)).

### 4.1.4 Comparison with NavCam

During LGA, 5 NavCam Moon observations were performed with a single mode acquisition but only 3 were on the illuminated surface, at the terminator, over Mare Fecunditatis and at the limb (Cornet et al., 2026). And only the second one over Mare Fecunditatis overlaps MAJIS footprint in its lower left corner (Figure 15). Unfortunately, this area is too limited to provide any

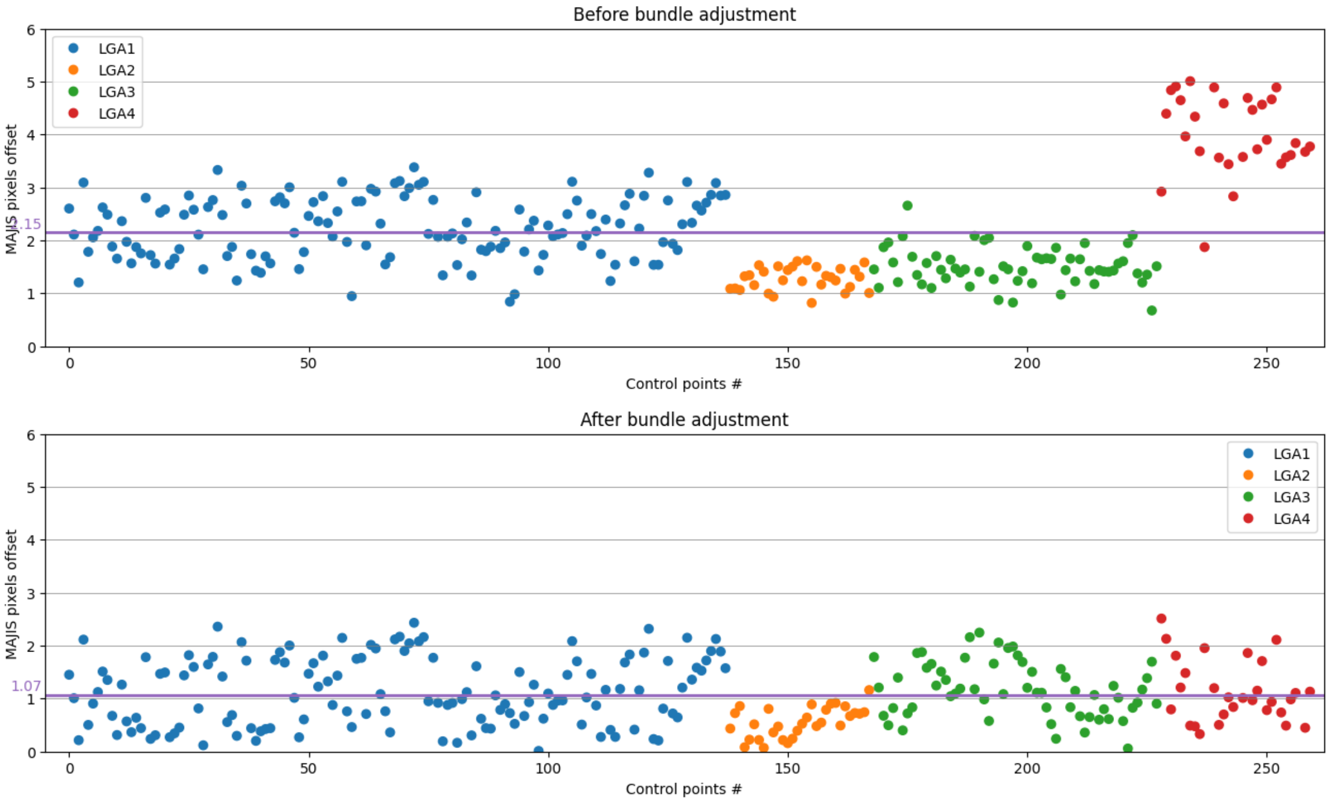

**Figure 14.** Control points residuals before (top) and after (bottom) bundle adjustment between MAJIS and JANUS. Units are in MAJIS IFOV.

additional constrain on MAJIS alignment. Nonetheless, it nicely illustrates that NavCam could be used as a valuable context camera for MAJIS (especially in windowing modes) when the scan angle larger than JANUS coverage (-0.3° to +1.0°) and provide an overlap between -1.7° up to +2.3°. A few seconds of difference in NavCam acquisition start time could have been significantly increased the relative coverage between MAJIS and NavCam. To get the best synergy between MAJIS, JANUS and NavCam, it is thus desirable to synchronize their observations, whenever possible to maximize common coverage.

## 4.2 Earth gravity assist (EGA)

### 4.2.1 Acquisition geometry

During the Earth flyby, 19 MAJIS observations were planned, 4 on the night-side, illuminated by the Moon light over South Asia; one at the terminator crossing over the Philippines, 12 on the dayside over the Pacific Ocean showing mainly cloud features, and two at the limb without any surface feature (see table 1 and figure 5 in Poulet et al. (2026) for more details). Similarly to the Moon, only the surface cubes will be considered in this study. They are labelled EGA1 to EGA17 (Figure 16).

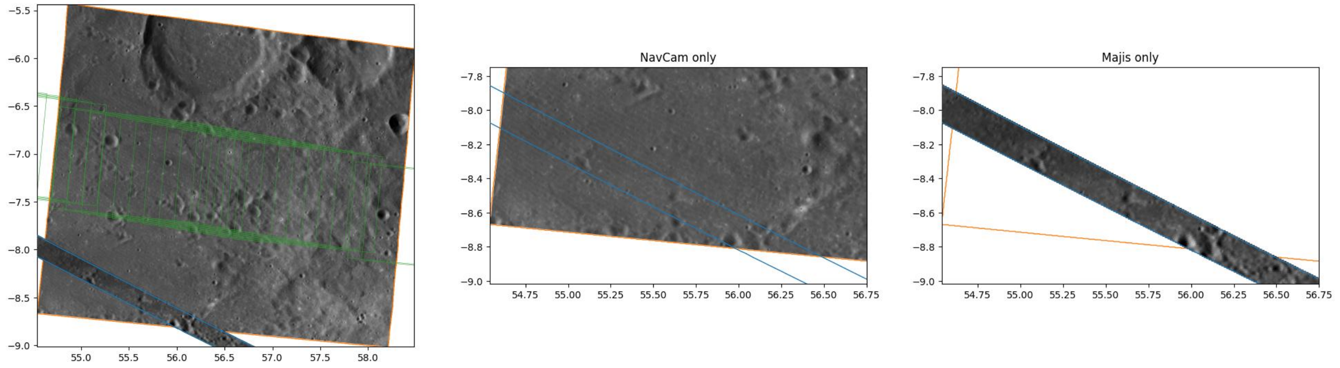

**Figure 15.** Left: Overview of the NavCam image (contoured in orange) and MAJIS image at 1.4 $\mu$m (contoured in blue) acquired over Mare Fecunditatis. JANUS footprints were added for reference (green). Center: Zoom on NavCam image only, with MAJIS footprint (blue). Right: Zoom on MAJIS image only, with NavCam footprint (orange).

Due to the very short exposure time, the observations where performed with 64-samples windowing, except EGA1 and EGA2 where a 128-samples windowing was used.

Dedicated analyses of this MAJIS dataset on Earth were performed and show an excellent agreement with Earth orbiting satellites measurements (PRISMA, IASI and ENMAP) covering the same locations (Oliva et al., 2026; Guerlet et al., 2026; Hueso et al., 2026). MAJIS was also able to detect spectroscopic signal of lightning (D'Aversa et al., 2026). Similarly to the Moon, JANUS observed the Earth continuously (Tubiana et al., 2026; Hueso et al., 2026), overlapping MAJIS footprints 4 times on the nightside and 11 times on the dayside. NavCam performed 9 observations, but only 2 of them are relevant for MAJIS (Cornet et al., 2026).

In order to assess the validity of MAJIS data georeferentiation on Earth (post-PC2 alignment), we conducted different analyses: (1) at the global scale with Earth weather satellites, (2) on the few visible islands, (3) on MAJIS overlaps, (4) between MAJIS and JANUS, (5) between MAJIS and NavCam.

It should be noted that in this section, contrary to the Moon's case, we did not ortho-rectify the images and only assumed that the line of sight will intersect the Earth ellipsoid, since most of MAJIS observations were above the ocean and the effective topography will be driven by the clouds. JANUS and NavCam were not ortho-rectified as well.

### 4.2.2 Global comparison with weather satellites

Weather satellites monitor the clouds evolution on Earth at high spatial resolution, at global scale, multiple times per hour (typical every 10 to 15 minutes). These datasets are particularly useful to extract the cloud context when MAJIS performed its observations (Figure 16). In our case, we use the image taken at 2024-08-20 21:30 above South Asia by the Advanced Himawari Imager (AHI) onboard Himawari-9 (JMA/MSC, 2021). The nightside clouds signature at 3.9 $\mu$m can be directly compared with MAJIS measurements at the same wavelength (EGA1 to EGA4). In term of geometry, all the cloud features are recognizable in both datasets and are well collocated at the global scale. On the day side, MAJIS cloud features (EGA5 to

EGA12) can also be correlated with the clouds observed in the visible channel. Here, we took advantage of the image taken at 2024-08-20 21:50 by the Advanced Baseline Imager (ABI) onboard GOES-18 (NOAA, 2022) to complete the cloud coverage over the Pacific (EGA13 to EGA17). Globally, MAJIS geometry on Earth is correct from one edge of the scan to the other and in both scanning directions.

### 4.2.3 Visible lands on Earth

Most of MAJIS images are either covered with clouds or over the ocean. After close inspection, we only found 5 distinct islands (in EGA4 and EGA5) that can be identified (Figure 17). All of them are located on the nightside, and their coastlines were retrieved thanks to the land/water thermal contrast at 4.6 $\mu$m in the infrared channel. The coordinates of the islands were extracted from CartoPy coastlines features (Met Office, 2010 - 2015) and compared with MAJIS observations. The alignment post-PC2 is slightly offset compared to expectation, however, by adding a small temporal shift of -1.6 and -1.0 seconds on EGA4 and EGA5 acquisition time respectively, we were able to recover most of the mismatch. The offset corresponds to misalignment of 7 and 4 samples along slit respectively. In the case of EGA5, we had to add a scan angle offset of -0.023°, corresponding to -2.7 slits, to better match all the islands.

In these cases, the resulting error is slightly larger than that observed on the Moon but all the observed features could still be readily matched. At this stage the discrepancy can likely be attributed to both the temporal shift and the scan-angle offset. Similar effects are also observed in other cases detailed afterwards (Table 5).

### 4.2.4 MAJIS overlaps

On two occasions, MAJIS was able to image by itself the same area in two consecutive observations (Figure 18). The first opportunity (EGA11 - EGA12) happened when the right side of the slit was acquired in a descending scan, then the next ascending scan on the left part of the slit crossed over the previous swath. When we extract the contours of the visible clouds contained in the overlapping area, we can directly compare the offset between the two acquisitions. In this case, a temporal positive shift of 0.5 seconds to the first observation and 0.05 seconds to the second one are sufficient to get the best match between the two observations.

During the second opportunity (EGA16 - EGA17), the two observations were performed with the same descending scan direction but this time, the first one was acquired in the center of the slit whereas the second one was on the left part of the slit. In this case, we can see that we had to time shift the first observation by 0.5 seconds to get an excellent match between the two cloud contours.

In both cases, the temporal shift is significantly smaller than the one observed on the visible islands (Table 5) and is equivalent to 2 samples along the slit which is consistent with the values obtained on the Moon before bundle adjustment.

Here, we assume that the parallax induced by the drift of the spacecraft between the observations does not affect significantly the comparison of cloud edges in the two viewing geometries (about 50 m for a 1 km cloud altitude).

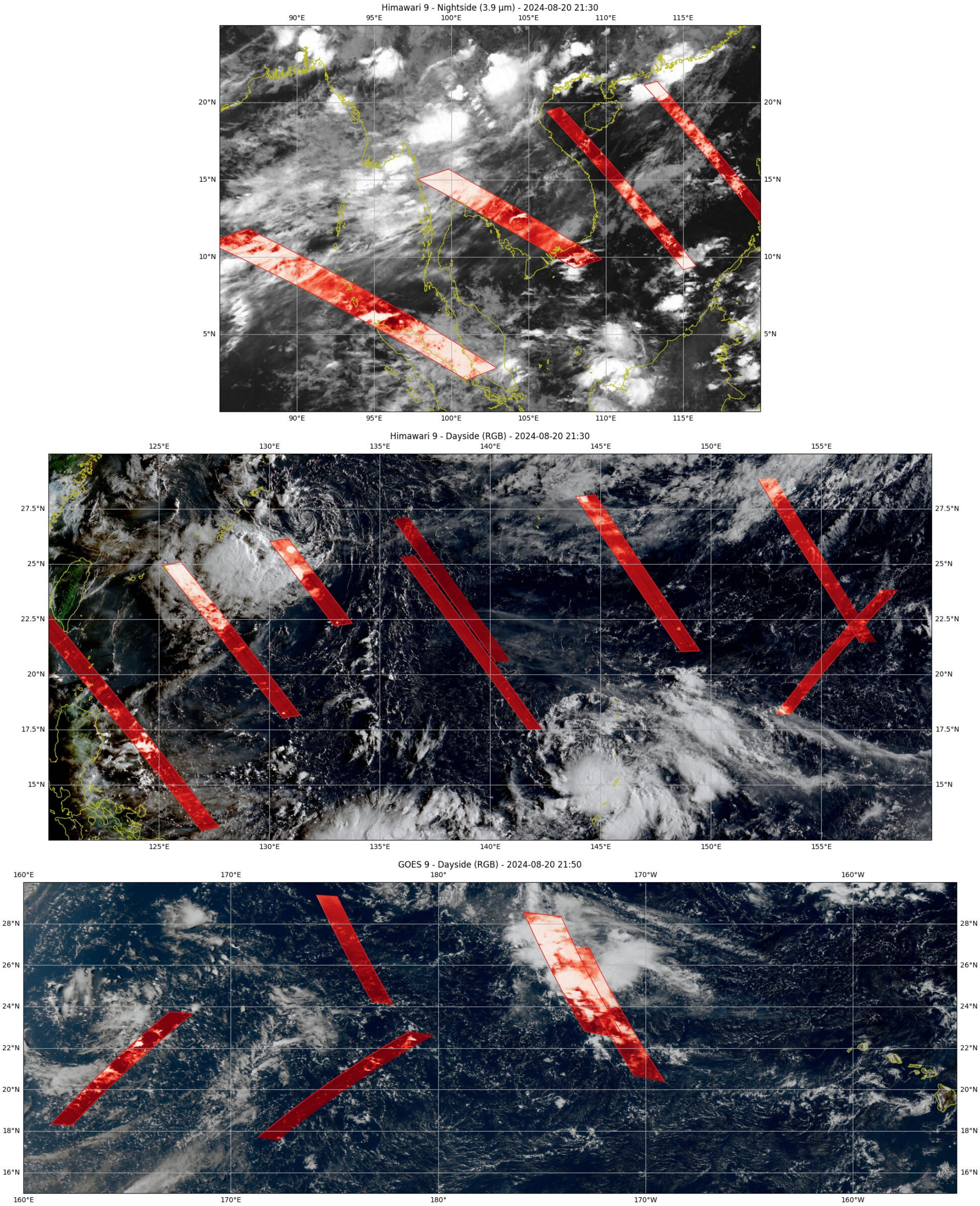

**Figure 16.** Comparison between the 17 MAJIS observations acquired during EGA (in red) and the clouds coverage recorded by two weather satellites (Himawari-9 and GOES-18) around the same time as MAJIS (21:30 and 21:50 respectively on 2024-08-20). Top panel: Himawari-9 nightside at 3.9 $\mu$m, with EGA1 to EG4 at 3.9 $\mu$m. Center panel: Himawari-9 dayside as true color (though Red, Green, Blue filters), with EGA5 to EGA12 at 3.9 $\mu$m. Bottom panel: GOES-18 dayside as true color (though Veggie, Red, Blue filters), with EGA13 to EGA17 at 3.9 $\mu$m. The coastlines are represented with yellow lines.

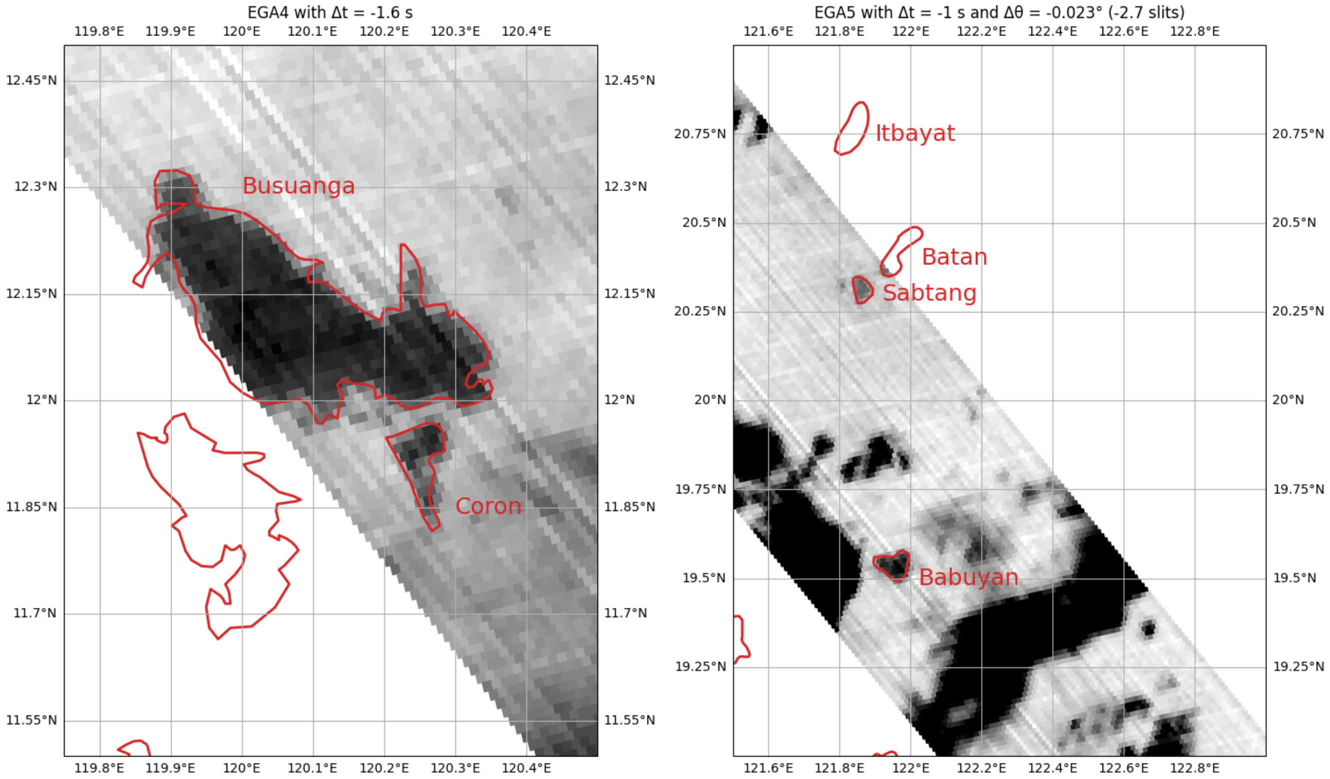

**Figure 17.** Comparison between isolated islands (in red) visible with MAJIS at 4.6 $\mu$m in EGA4 (left) and (EGA5). In both cases, we observe a temporal shift ($\Delta$t) between the observed signal and the expected islands location. In the case of EGA5, in order to minimize the offset, it is required to add additional scan offset ($\Delta\theta$).

### 4.2.5 Comparison with JANUS

As mentioned before, almost all MAJIS observations on Earth overlap JANUS footprints (except EGA7 and EGA13). However, JANUS night-side observations do not have enough contrast to perform a good comparison with MAJIS. Therefore, we will only focus our attention to the overlap occurring on the dayside (EGA5 to EGA17). Figure 19 shows a summary of the three of these opportunities (the rest of the opportunities are available in Figure A1 in appendix). In all cases we were able to match the MAJIS data with the JANUS images. We first extracted cloud boundaries from JANUS and performed a manual alignment by adjusting temporal shift and scan offset to minimize the misalignment (Table 5). On average, the temporal shift is -1.1 ± 0.6 s (equivalent to -4.7 ± 2.5 samples) and the scan offset is 0.085 ± 0.018° (10.0 ± 2.1 IFOV). These values are significantly larger than those reported previously and the cause of this difference is still under investigation. Nevertheless, these two parameters are sufficient to obtain an almost perfect alignment.

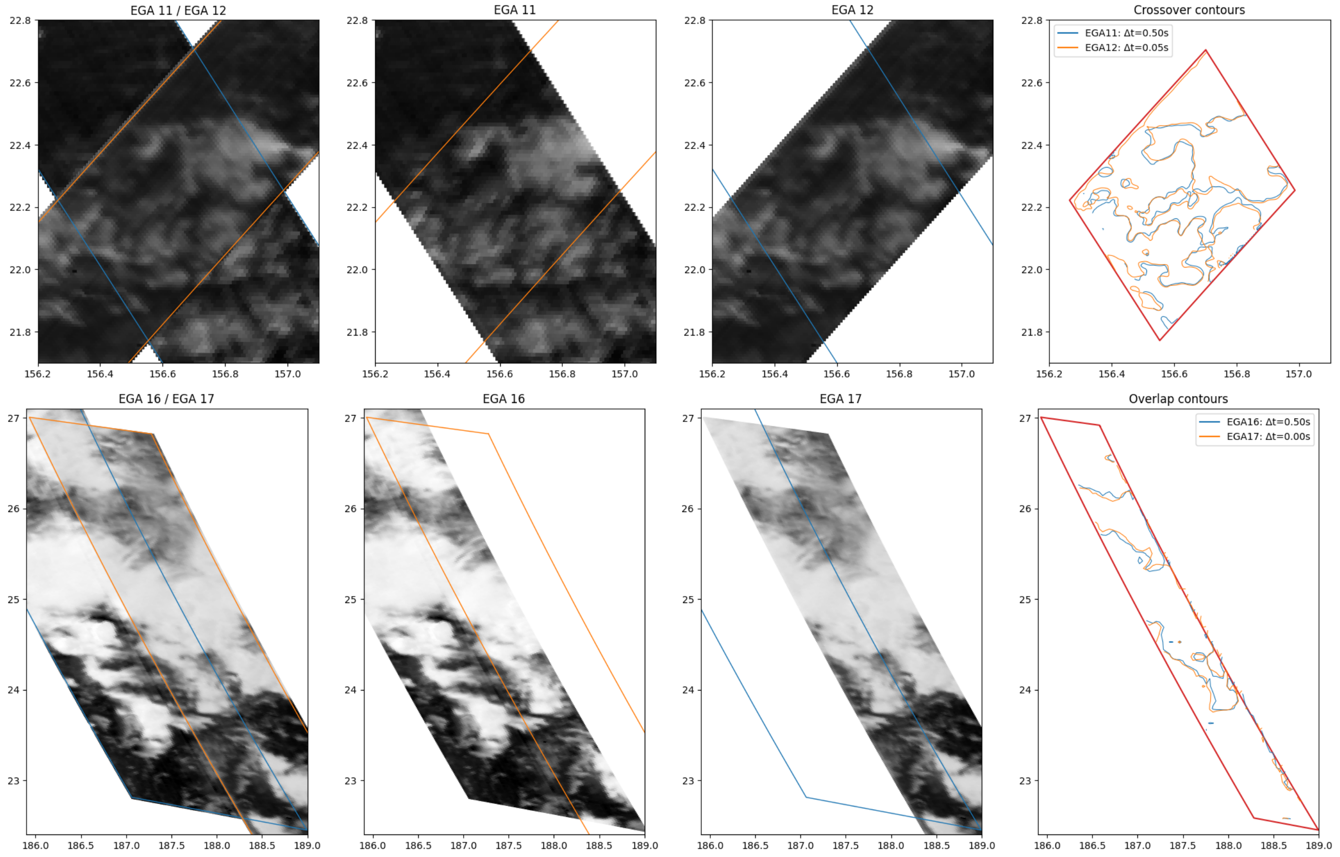

**Figure 18.** Top panels: MAJIS EGA11 and EGA12 crossover with opposite scan directions. EGA11 is acquired on the right side of the slit, while EGA12 is acquired on the left. Bottom panels: MAJIS EGA16 and EGA17 overlap with identical scan directions. EGA16 is acquired in the middle of the slit and EGA17 on the left part. In both cases, the projections shown in the three left panels are based on the PC2 alignment. The right panel provides a comparison between the detected contours in both images after adjustment with a time offset ($\Delta$t) to minimize the misalignment. No scan offset has been applied. The images are displayed at 3.9 $\mu$m.

https://doi.org/10.5194/egusphere-2026-2655
Preprint. Discussion started: 20 May 2026

**Table 5.** Summary of MAJIS residual time shift (Δt) and scan offsets (Δ$\theta$) measured to overlap the observations with other datasets.

| MAJIS observation | Comparison with | Δt | Δ$\theta$ |
|---|---|---|---|
| EGA4 | Island contours (CartoPy) | -1.6 s | |
| EGA5 | Island contours (CartoPy) | -1.0 s | -0.023° |
| EGA11 | MAJIS EGA12 | 0.45 s | |
| EGA16 | MAJIS EGA17 | 0.50 s | |
| EGA5 | JANUS (21:34:55) | -1.8 s | 0.055° |
| EGA6 | JANUS (21:36:21) | -1.6 s | 0.06° |
| EGA8 | JANUS (21:39:00) | -1.4 s | 0.065° |
| EGA9 | JANUS (21:39:00) | -2.0 s | 0.075° |
| EGA10 | JANUS (21:40:47) | -1.2 s | 0.08° |
| EGA11 | JANUS (21:42:36) | -0.7 s | 0.1° |
| EGA12 | JANUS (21:43:12) | -1.2 s | 0.1° |
| EGA14 | JANUS (21:47:13) | -0.3 s | 0.1° |
| EGA15 | JANUS (21:46:37) | -0.6 s | 0.1° |
| EGA16 | JANUS (21:48:25) | -0.4 s | 0.1° |
| EGA17 | JANUS (21:48:25) | -0.5 s | 0.1° |
| EGA10 | NavCam (21:27:11) | | 0.05° |

### 4.2.6 Comparison with NavCam

Similarly to the Moon's case, NavCam observations on the Earth were performed in a single acquisition mode (Cornet et al., 2026). However, this time, the number of overlaps with MAJIS is larger (5 images vs. 1 on the Moon). Unfortunately, two of those image are saturated, one is underexposed, leaving only two useful opportunities that overlap MAJIS (Figure 20).

The first overlap occurs on the nightside with EGA1 observation, on the exact same location where MAJIS observed spectroscopic signal of lightning (D'Aversa et al., 2026) and very fortunately, NavCam also observed a very bright flash on the same cloud at a close-by location. Since NavCam was only illuminated by the Moon shine, its exposure time was longer than its dwell time, leading to image smearing. Nevertheless, the location and the shape of the cloud is still consistent between NavCam and MAJIS with MAJIS being able to recover more details in the cloud structures than NavCam. This unique case nicely demonstrates the complementarity of the two instruments.

The second overlap occurs on the dayside with EGA10 observation. It is possible to clearly identify the same features between the two images with only a 0.05° scan offset (5 IFOV) to realign the cloud contours (Table 5). We also note that a comparable level of detail can be retrieved from both datasets, with NavCam providing a larger field of view.

https://doi.org/10.5194/egusphere-2026-2655
Preprint. Discussion started: 20 May 2026

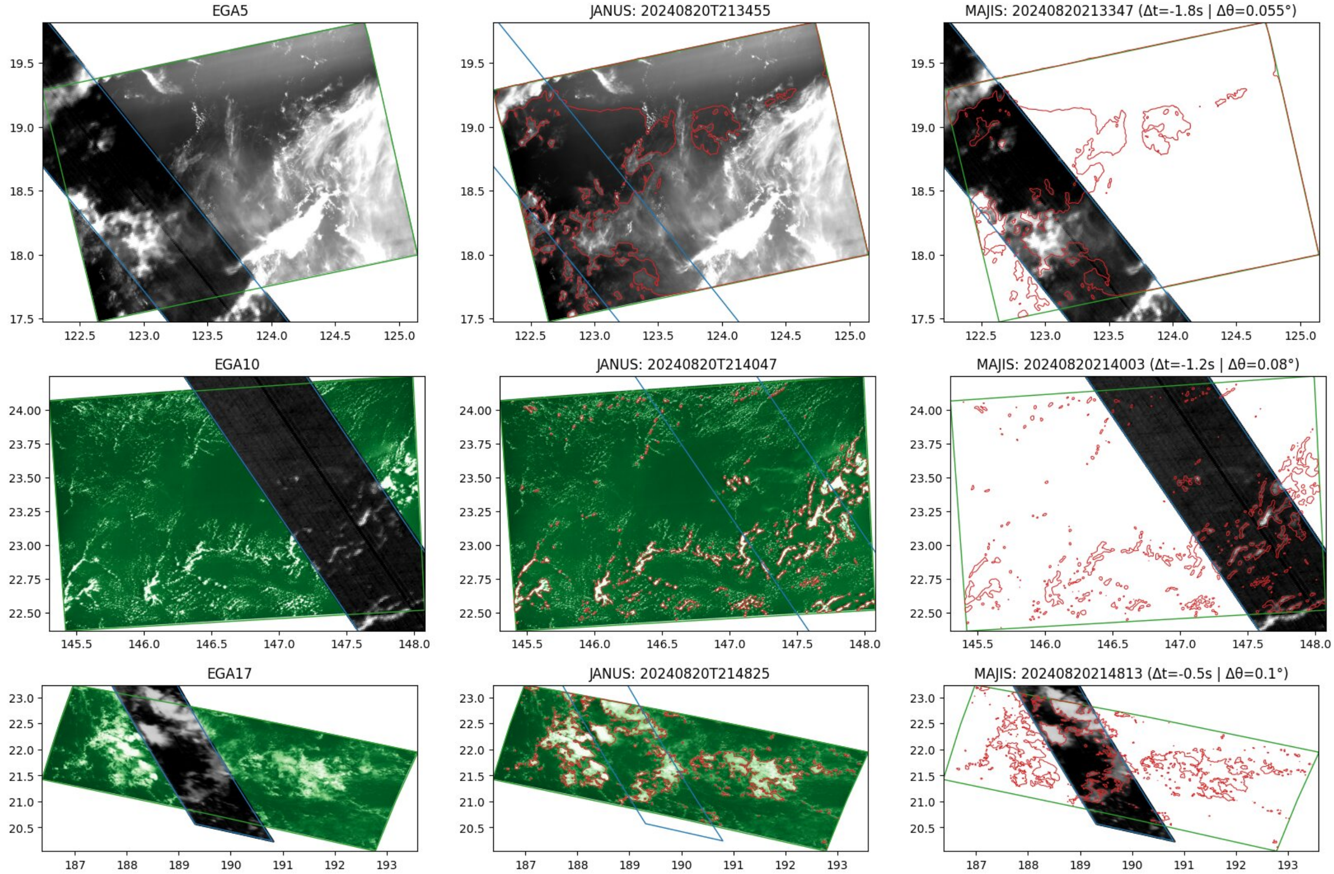

**Figure 19.** Three comparisons (EGA5, EGA10 and EGA17) between the clouds observed by MAJIS (3.9 $\mu$m) and JANUS (panchromatic or green filters) on the dayside. MAJIS is contoured in blue and JANUS is contoured in green. The clouds edges (in red) are detected on JANUS images (center) and reported on MAJIS images (right). To minimize the offset, a temporal shift (Δt) and a scan offset ($\Delta\theta$) are applied.

## 5 Conclusions and perspectives

In this work, we provided an overview of MAJIS optical path, from the VISNIR and IR detectors pixels layout, to the spaxel readout, the binning and windowing modes, as well as the conversion of internal mirror motion into viewing scan angles. The different instrument units were decomposed into their relevant SPICE frames in order to establish their mutual relationships, resulting into the MAJIS extended field of view, which correspond to the total field accessible to MAJIS. We use the data collected during in-flight checkout session PC2 on two starfields to assess the instrument geometric calibration after the launch. During these two observations, 14 stars were detected and their centroids were located with sub-spaxel accuracy. Compared to the Gaia DR3 star catalog, the initial ground calibration showed an average offset of 6.5 IFOV. To reduce this misalignment, a new TKFRAME between the SPACECRAFT and MAJIS BASE frame was computed and led to a new misalignment of 0.7 IFOV. This new value will be reported in the MAJIS frame and instrument SPICE kernels, allowing a direct comparison

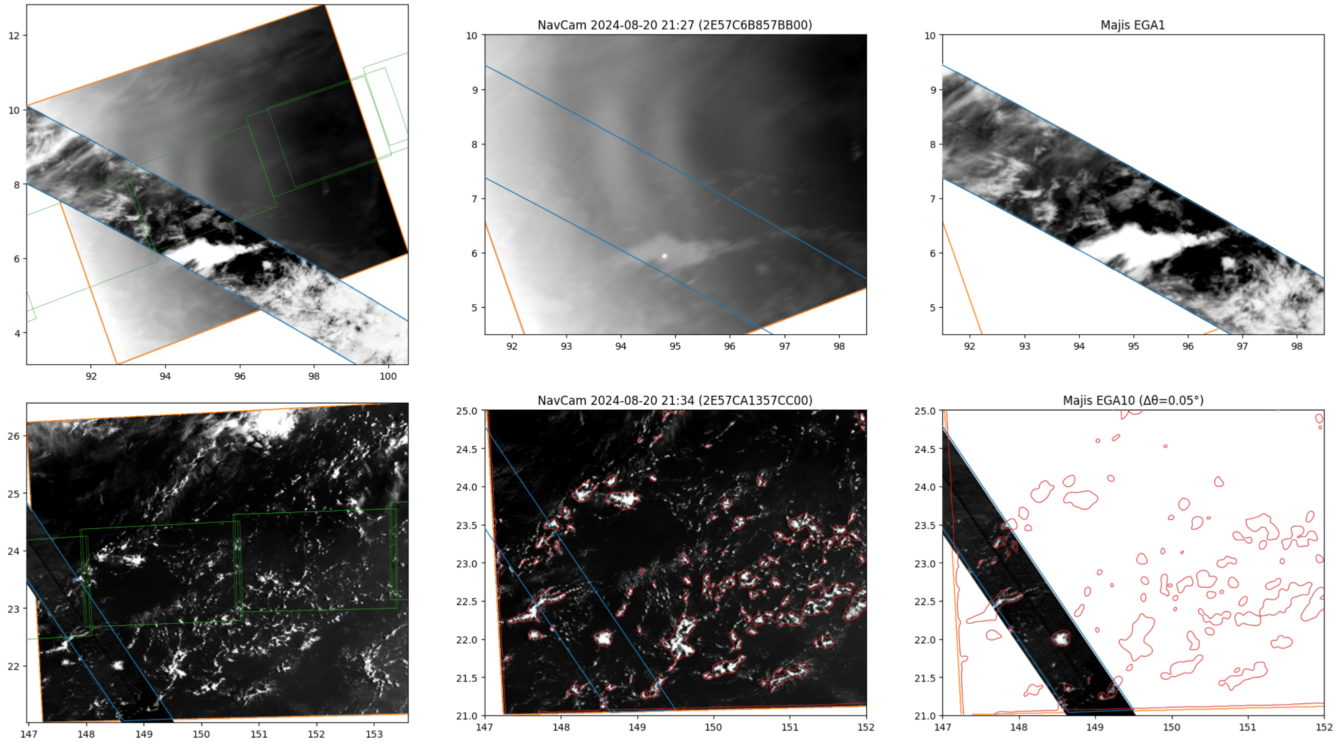

**Figure 20.** Left: Comparisons of MAJIS (EGA1 and EGA10 outlined in blue) images at 3.9 $\mu$m with overlapping NavCam images (outlined in orange) on the night (upper panel) and dayside (lower panel) respectively. JANUS footprints are added for reference in green. Center: Zoom on NavCam images only, with the MAJIS footprint overlaid in blue. Right: Zoom on MAJIS images only, with the NavCam footprint overlaid in orange. No offset correction was applied on EGA1, whereas a scan offset ($\Delta\theta$) was added to EGA10 to minimize the offset (aligned with the red cloud contours from NavCam).

between MAJIS boresight and the spacecraft +Z axis, which are 27 samples and 31 lines apart. We also provided the relative offset with the other Juice remote sensing instruments.

Then, we use MAJIS LGA and EGA observations to verify the accuracy of this new alignment. On the Moon, compared to JANUS, the average error in the central part of the scan (-0.3° to +1.0°) is about 2 IFOV and could be improved down to 1 IFOV with a bundle adjustment. Due to their relatively small overlap, the comparison with NavCam is consistent but remains limited. On Earth, we were able to match all the MAJIS data at global scale with two weather satellites observing at nearly the same time. In this case the full extent of the field of view was used and confirm the overall good alignment of MAJIS data. We were also able to detect a few small islands within 3 to 7 IFOV. In two occurrences, MAJIS was able to overlap its own observations showing a good self-alignment (about 2 IFOV), consistent with the Moon retrievals. Finally, comparisons with JANUS and NavCam were performed and showed residual offsets of 5 to 10 IFOV in the worst case. These larger offsets are still under investigation, however, adjusting a temporal shift and/or a scan offset is sufficient to make all these datasets are very well co-aligned.

About SPICE kernels distribution, due to the limited number of stars detected during PC2, the values derived for most spatial calibration parameters during ground calibration have been maintained after this first in-flight calibration study. The relative rotation between the SPACECRAFT and MAJIS BASE frames, which is critical for the relationship with the spacecraft reference frame and for cross-calibration with other instrument, has been updated (with new TKFRAME values). Additional in-flight observations are considered before arrival at Jupiter for adjusting additional parameters, e.g. the relative offset the between the internal mirror rotation axis and the slit primary direction (at present considered as aligned), the relative orientation between VISNIR and IR channels with respect to the slit, or the linearity relationship between the mirror steps and the viewing scan angles. As we saw for the Earth's case, the timing of the acquisitions will need to be further analyzed, since the acquired starfields during PC2 do not provide any timing constraints. Additional pointing campaigns are planned during the cruise phase (1 per year up to 2030). One of them, PC4, was just collected in February 2026 and should provide additional insights. Even though, these observations were performed successfully, at the time of writing, their analysis is still on-going and the results cannot be included in this paper. During the nominal science phase, we may need to regularly check the instrument alignment. Since these observations require a large amount of data volume, they could only a few of them will be performed during the operational phase.

This analysis provided a few interesting lessons learned. First, early in-flight geometric calibration is essential to assess the instrument field of view and pointing capabilities as soon as possible after launch. Our results show that MAJIS has a good initial alignment and only simple adjustments are sufficient to achieve optimal co-alignment with the other remote sensing instruments, down to IFOV scale. Distribution of the new alignment parameters through the SPICE kernels dataset is essential to ensure a widespread and tracked update, among the MAJIS team and with the other instrument teams to improve synergetic observations. Finally, when MAJIS operates in windowing modes, it is highly recommended to request a support from JANUS and/or NavCam to provide additional context to these observations and if necessary, correct any remaining off-pointing. These observations need to be synchronized, whenever possible, to maximize common coverage.

*Author contributions.*

BS led the analysis and writing of the manuscript. FP and YL supervised the project. EDA, NL, CD, MM, CL, SJ, SLM, GT, NM, GP, FT, KS contributed to MAJIS operations and data processing. PP, LA, LP, LLD provided the JANUS dataset and advices to support this analysis. TC, IB, MCS, AE provided the NavCam dataset and advices to support this analysis. SS contributed to the weather satellite analysis. All the authors reviewed and edited the manuscript.

*Competing interests.*

The authors declare no competing interests.

*Acknowledgements.* This work was supported by CNES, focused on MAJIS. This work has been developed under the ASI-INAF agreement no. 2023-6-HH.0. The authors also wish to thank ESA teams from SOC, MOC and ESTEC, as well as Airbus Defence and Space for their technical and operational support to the MAJIS project. Juice is a mission under ESA leadership with contributions from its Member States, NASA, JAXA and ISA. It is the first Large-class mission in ESA's Cosmic Vision programme.

This work has made use of data from the European Space Agency (ESA) mission Gaia, processed by the Gaia Data Processing and Analysis Consortium (DPAC). Funding for the DPAC has been provided by national institutions, in particular the institutions participating in the Gaia Multilateral Agreement.

The authors would like to thank all the contributors to the following python libraries heavily used in this study: Numpy (Harris et al., 2020), Matplotlib (Hunter, 2007), Scipy (Virtanen et al., 2020), SpiceyPy (Annex et al., 2020), Planetary-Coverage (Seignovert et al., 2025), CartoPy (Met Office, 2010 - 2015) and SatPy (Martin Raspaud et al., 2026).

*Code and data availability.* The MAJIS raw (PSA, 2029b) and calibrated (PSA, 2029a) archive data are currently under embargo but are scheduled to be released in 2029 in the ESA Planetary Science Archive (PSA) (Besse et al., 2018) six months after Earth Gravity Assist #3. All the source code to reproduce the results in this article will be available on Nantes University Gitlab and will be archived in Software Heritage.

**Table A1.** For simplicity, all the MAJIS observations during LGA and EGA are described in this paper with their flyby id instead of their acquisition time. Here is corresponding table to properly identify the MAJIS products in the archive.

| MAJIS flyby id | Acquisition time | Samples | Lines | Slit position | Scan direction | Comment |
|---|---|---|---|---|---|---|
| LGA1 | 20240819211816 | 400 | 99 | Full | Fixed | Terminator |
| LGA2 | 20240819211923 | 64 | 1,274 | Middle | Descending | Dayside |
| LGA3 | 20240819212141 | 64 | 1,269 | Middle | Descending | Dayside |
| LGA4 | 20240819212402 | 64 | 841 | Left | Descending | Dayside |
| LGA5 | 20240819212539 | 64 | 535 | Right | Descending | Limb (not used) |
| EGA1 | 20240820212509 | 128 | 865 | Middle | Descending | nightside |
| EGA2 | 20240820212818 | 128 | 580 | Middle | Descending | nightside |
| EGA3 | 20240820213029 | 64 | 850 | Middle | Descending | nightside |
| EGA4 | 20240820213208 | 64 | 850 | Middle | Descending | nightside |
| EGA5 | 20240820213347 | 64 | 890 | Middle | Descending | Terminator |
| EGA6 | 20240820213530 | 64 | 600 | Middle | Descending | Dayside |
| EGA7 | 20240820213644 | 64 | 330 | Middle | Descending | Dayside |
| EGA8 | 20240820213731 | 64 | 550 | Right | Descending | Dayside |
| EGA9 | 20240820213840 | 64 | 690 | Left | Descending | Dayside |
| EGA10 | 20240820214003 | 64 | 600 | Middle | Descending | Dayside |
| EGA11 | 20240820214117 | 64 | 600 | Right | Descending | Dayside |
| EGA12 | 20240820214231 | 64 | 600 | Left | Ascending | Dayside |
| EGA13 | 20240820214350 | 64 | 650 | Middle | Ascending | Dayside |
| EGA14 | 20240820214509 | 64 | 650 | Right | Ascending | Dayside |
| EGA15 | 20240820214628 | 64 | 380 | Left | Descending | Dayside |
| EGA16 | 20240820214720 | 64 | 380 | Middle | Descending | Dayside |
| EGA17 | 20240820214813 | 64 | 410 | Left | Descending | Dayside |
| EGA18 | 20240820214909 | 64 | 600 | Right | Descending | Limb (not used) |
| EGA19 | 20240820215024 | 128 | 300 | Middle | Descending | Limb (not used) |

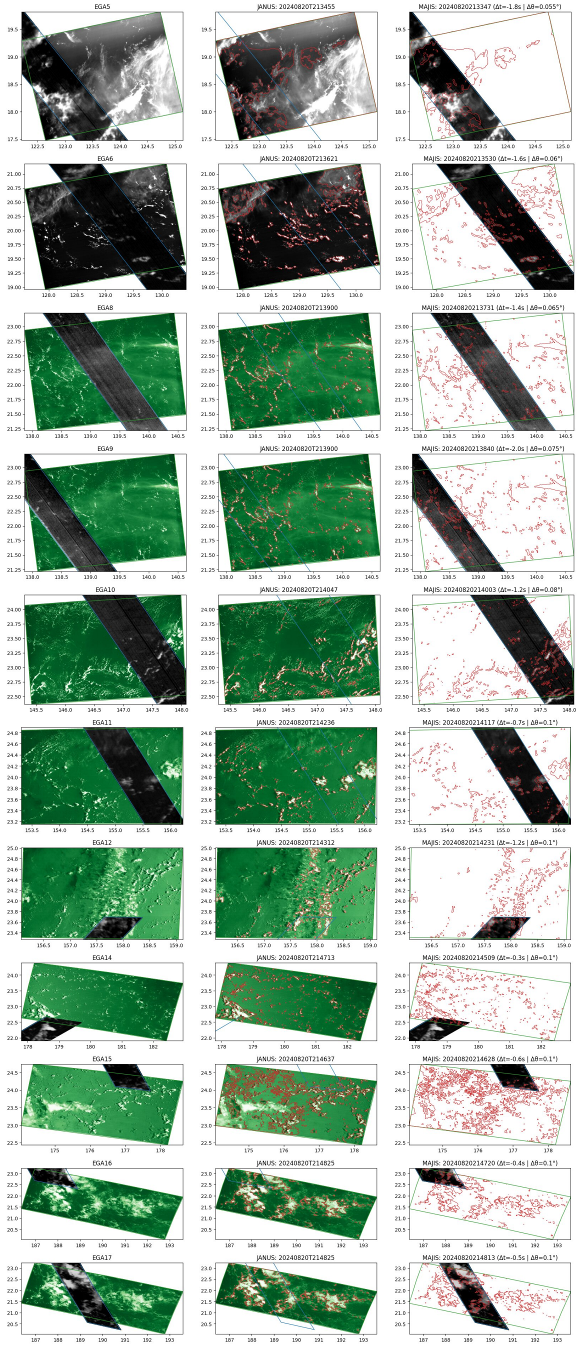

**Figure A1.** Complementary figure to Figure 19 for all MAJIS (3.9 $\mu$m) dayside observation (EGA5 to EGA17) overlapping JANUS images (panchromatic or green filters) on the dayside. MAJIS is contoured in blue and JANUS is contoured in green. The cloud edges (in red) are detected on JANUS images (center) and reported on MAJIS images (right). To minimize the offset, a temporal shift ($\Delta$t) and a mirror offset ($\Delta\theta$) is required on all cases.

https://doi.org/10.5194/egusphere-2026-2655
Preprint. Discussion started: 20 May 2026

## References

Acton, C., Bachman, N., Semenov, B., and Wright, E.: A look towards the future in the handling of space science mission geometry, Planetary and Space Science, 150, 9–12, https://doi.org/10.1016/j.pss.2017.02.013, 2018.

Acton, C. H.: Ancillary data services of NASA's Navigation and Ancillary Information Facility, Planetary and Space Science, 44, 65–70, https://doi.org/10.1016/0032-0633(95)00107-7, planetary data system, 1996.

Agostini et al.: Calibrating JANUS: an overview of the calibration pipeline and what we learned from the Moon-Earth flyby data, Annales Geophysicae, 2026.

Annex, A., Pearson, B., Seignovert, B., Carcich, B., Eichhorn, H., Mapel, J., von Forstner, J., McAuliffe, J., del Rio, J., Berry, K., Aye, K.-M., Stefko, M., de Val-Borro, M., Kulumani, S., and Murakami, S.-y.: SpiceyPy: a Pythonic Wrapper for the SPICE Toolkit, Journal of Open Source Software, 5, 2050, https://doi.org/10.21105/joss.02050, 2020.

Besse, S., Vallat, C., Barthelemy, M., Coia, D., Costa, M., De Marchi, G., Fraga, D., Grotheer, E., Heather, D., Lim, T., Martinez, S., Arviset, C., Barbarisi, I., Docasal, R., Macfarlane, A., Rios, C., Saiz, J., and Vallejo, F.: ESA's Planetary Science Archive: Preserve and present reliable scientific data sets, Planetary and Space Science, 150, 131–140, https://doi.org/10.1016/j.pss.2017.07.013, 2018.

Boutonnet, A., Langevin, Y., and Erd, C.: Designing the JUICE Trajectory, Space Science Reviews, 220, https://doi.org/10.1007/s11214-024-01093-y, 2024.

Cornet, T., Tissot-Favre, A., Belgacem, I., Vallejo, F., Escalante Lopez, A., Andres, R., Witasse, O., Vallat, C., and Altobelli, N.: The JMC and NAVCAM cameras on the ESA JUICE spacecraft, Tech. rep., Copernicus Meetings, https://doi.org/10.5194/egusphere-egu26-20758, 2026.

Dietz, A., Boutonnet, A., and Budnik, F.: The JUICE Lunar-Earth gravity assist from trajectory design, navigation and spacecraft operations perspective, Annales Geophysicae, https://doi.org/10.5194/egusphere-2026-1015, 2026.

D'Aversa, E., Oliva, F., Piccioni, G., Poulet, F., Kolmašová, I., Migliorini, A., Filacchione, G., Fletcher, L., Mura, A., Langevin, Y., Seignovert, B., Grassi, D., Rodriguez, S., Tosi, F., Ligier, N., Sindoni, G., Giardino, M., and Plainaki, C.: Spectroscopic detection of terrestrial lightning from space by JUICE-MAJIS during Earth Gravity Assist, Annales Geophysicae, https://doi.org/10.5194/egusphere-2025-6453, 2026.

ESA SPICE Service: Juice SPICE Kernel Dataset, https://doi.org/10.5270/esa-ybmj68p, 2019.

Filacchione, G., Haffoud, P., Poulet, F., Piccioni, G., Langevin, Y., Tommasi, L., Barbis, A., Carter, J., Guerri, I., Dumesnil, C., De Angelis, S., Vincendon, M., Stefani, S., Pilorget, C., Tosi, F., and Rodriguez, S.: Calibration of MAJIS (Moons And Jupiter Imaging Spectrometer). II. Spatial calibration, Review of Scientific Instruments, 95, https://doi.org/10.1063/5.0203872, 2024.

Gaia Collaboration, Vallenari, A., Brown, A. G. A., Prusti, T., de Bruijne, J. H. J., Arenou, F., Babusiaux, C., Biermann, M., Creevey, O. L., Ducourant, C., Evans, D. W., Eyer, L., Guerra, R., Hutton, A., Jordi, C., Klioner, S. A., Lammers, U. L., Lindegren, L., Luri, X., Mignard, F., Panem, C., Pourbaix, D., Randich, S., Sartoretti, P., Soubiran, C., Tanga, P., Walton, N. A., Bailer-Jones, C. A. L., Bastian, U., Drimmel, R., Jansen, F., Katz, D., Lattanzi, M. G., van Leeuwen, F., Bakker, J., Cacciari, C., Castañeda, J., De Angeli, F., Fabricius, C., Fouesneau, M., Frémat, Y., Galluccio, L., Guerrier, A., Heiter, U., Masana, E., Messineo, R., Mowlavi, N., Nicolas, C., Nienartowicz, K., Pailler, F., Panuzzo, P., Riclet, F., Roux, W., Seabroke, G. M., Sordo, R., Thévenin, F., Gracia-Abril, G., Portell, J., Teyssier, D., Altmann, M., Andrae, R., Audard, M., Bellas-Velidis, I., Benson, K., Berthier, J., Blomme, R., Burgess, P. W., Busonero, D., Busso, G., Cánovas, H., Carry, B., Cellino, A., Cheek, N., Clementini, G., Damerdji, Y., Davidson, M., de Teodoro, P., Nuñez Campos, M., Delchambre, L., Dell'Oro, A., Esquej, P., Fernández-Hernández, J., Fraile, E., Garabato, D., García-Lario, P., Gosset, E., Haigron, R., Halbwachs, J.-L., Hambly, N. C., Harrison, D. L., Hernández, J., Hestroffer, D., Hodgkin, S. T., Holl, B., Janßen, K., Jevardat de Fombelle, G., Jordan, S., Krone-Martins, A., Lanzafame, A. C., Löffler, W., Marchal, O., Marrese, P. M., Moitinho, A., Muinonen, K., Osborne, P., Pancino, E., Pauwels, T., Recio-Blanco, A., Reylé, C., Riello, M., Rimoldini, L., Roegiers, T., Rybizki, J., Sarro, L. M., Siopis, C., Smith, M., Sozzetti, A., Utrilla, E., van Leeuwen, M., Abbas, U., Ábrahám, P., Abreu Aramburu, A., Aerts, C., Aguado, J. J., Ajaj, M., Aldea-Montero, F., Altavilla, G., Álvarez, M. A., Alves, J., Anders, F., Anderson, R. I., Anglada Varela, E., Antoja, T., Baines, D., Baker, S. G., Balaguer-Núñez, L., Balbinot, E., Balog, Z., Barache, C., Barbato, D., Barros, M., Barstow, M. A., Bartolomé, S., Bassilana, J.-L., Bauchet, N., Becciani, U., Bellazzini, M., Berihuete, A., Bernet, M., Bertone, S., Bianchi, L., Binnenfeld, A., Blanco-Cuaresma, S., Blazere, A., Boch, T., Bombrun, A., Bossini, D., Bouquillon, S., Bragaglia, A., Bramante, L., Breedt, E., Bressan, A., Brouillet, N., Brugaletta, E., Bucciarelli, B., Burlacu, A., Butkevich, A. G., Buzzi, R., Caffau, E., Cancelliere, R., Cantat-Gaudin, T., Carballo, R., Carlucci, T., Carnerero, M. I., Carrasco, J. M., Casamiquela, L., Castellani, M., Castro-Ginard, A., Chaoul, L., Charlot, P., Chemin, L., Chiaramida, V., Chiavassa, A., Chornay, N., Comoretto, G., Contursi, G., Cooper, W. J., Cornez, T., Cowell, S., Crifo, F., Cropper, M., Crosta, M., Crowley, C., Dafonte, C., Dapergolas, A., David, M., David, P., de Laverny, P., De Luise, F., De March, R., De Ridder, J., de Souza, R., de Torres, A., del Peloso, E. F., del Pozo, E., Delbo, M., Delgado, A., Delisle, J.-B., Demouchy, C., Dharmawardena, T. E., Di Matteo, P., Diakite, S., Diener, C., Distefano, E., Dolding, C., Edvardsson, B., Enke, H., Fabre, C., Fabrizio, M., Faigler, S., Fedorets, G., Fernique, P., Fienga, A., Figueras, F., Fournier, Y., Fouron, C., Fragkoudi, F., Gai, M., Garcia-Gutierrez, A., Garcia-Reinaldos, M., García-Torres, M., Garofalo, A., Gavel, A., Gavras, P., Gerlach, E., Geyer, R., Giacobbe, P., Gilmore, G., Girona, S., Giuffrida, G., Gomel, R., Gomez, A., González-Núñez, J., González-Santamaría, I., González-Vidal, J. J., Granvik, M., Guillout, P., Guiraud, J., Gutiérrez-Sánchez, R., Guy, L. P., Hatzidimitriou, D., Hauser, M., Haywood, M., Helmer, A., Helmi, A., Sarmiento, M. H., Hidalgo, S. L., Hilger, T., Hładczuk, N., Hobbs, D., Holland, G., Huckle, H. E., Jardine, K., Jasniewicz, G., Jean-Antoine Piccolo, A., Jiménez-Arranz, Ó., Jorissen, A., Juaristi Campillo, J., Julbe, F., Karbevska, L., Kervella, P., Khanna, S., Kontizas, M., Kordopatis, G., Korn, A. J., Kóspál, Á., Kostrzewa-Rutkowska, Z., Kruszyńska, K., Kun, M., Laizeau, P., Lambert, S., Lanza, A. F., Lasne, Y., Le Campion, J.-F., Lebreton, Y., Lebzelter, T., Leccia, S., Leclerc, N., Lecoeur-Taibi, I., Liao, S., Licata, E. L., Lindstrøm, H. E. P., Lister, T. A., Livanou, E., Lobel, A., Lorca, A., Loup, C., Madrero Pardo, P., Magdaleno Romeo, A., Managau, S., Mann, R. G., Manteiga, M., Marchant, J. M., Marconi, M., Marcos, J., Marcos Santos, M. M. S., Marín Pina, D., Marinoni, S., Marocco, F., Marshall, D. J., Martin Polo, L., Martín-Fleitas, J. M., Marton, G., Mary, N., Masip, A., Massari, D., Mastrobuono-Battisti, A., Mazeh, T., McMillan, P. J., Messina, S., Michalik, D., Millar, N. R., Mints, A., Molina, D., Molinaro, R., Molnár, L., Monari, G., Monguió, M., Montegriffo, P., Montero, A., Mor, R., Mora, A., Morbidelli, R., Morel, T., Morris, D., Muraveva, T., Murphy, C. P., Musella, I., Nagy, Z., Noval, L., Ocaña, F., Ogden, A., Ordenovic, C., Osinde, J. O., Pagani, C., Pagano, I., Palaversa, L., Palicio, P. A., Pallas-Quintela, L., Panahi, A., Payne-Wardenaar, S., Peñalosa Esteller, X., Penttilä, A., Pichon, B., Piersimoni, A. M., Pineau, F.-X., Plachy, E., Plum, G., Poggio, E., Prša, A., Pulone, L., Racero, E., Ragaini, S., Rainer, M., Raiteri, C. M., Rambaux, N., Ramos, P., Ramos-Lerate, M., Re Fiorentin, P., Regibo, S., Richards, P. J., Rios Diaz, C., Ripepi, V., Riva, A., Rix, H.-W., Rixon, G., Robichon, N., Robin, A. C., Robin, C., Roelens, M., Rogues, H. R. O., Rohrbasser, L., Romero-Gómez, M., Rowell, N., Royer, F., Ruz Mieres, D., Rybicki, K. A., Sadowski, G., Sáez Núñez, A., Sagristà Sellés, A., Sahlmann, J., Salguero, E., Samaras, N., Sanchez Gimenez, V., Sanna, N., Santoveña, R., Sarasso, M., Schultheis, M., Sciacca, E., Segol, M., Segovia, J. C., Ségransan, D., Semeux, D., Shahaf, S., Siddiqui, H. I., Siebert, A., Siltala, L., Silvelo, A., Slezak, E., Slezak, I., Smart, R. L., Snaith, O. N., Solano, E., Solitro, F., Souami, D., Souchay, J., Spagna, A., Spina, L., Spoto, F., Steele, I. A., Steidelmüller, H., Stephenson, C. A., Süveges, M., Surdej, J., Szabados, L., Szegedi-Elek, E., Taris, F., Taylor, M. B., Teixeira, R., Tolomei, L., Tonello, N., Torra, F., Torra, J., Torralba Elipe, G., Trabucchi, M., Tsounis, A. T., Turon, C., Ulla, A., Unger, N., Vaillant, M. V., van Dillen, E., van Reeven, W., Vanel, O., Vecchiato, A., Viala, Y., Vicente, D., Voutsinas, S., Weiler, M., Wevers, T., Wyrzykowski, L., Yoldas, A., Yvard, P., Zhao, H., Zorec, J., Zucker, S., and Zwitter, T.: Gaia Data Release 3:

Summary of the content and survey properties, Astronomy &amp; Astrophysics, 674, A1, https://doi.org/10.1051/0004-6361/202243940, 2023.

Gorog, F., Arnolfo, M.-C., Belmana, S., Dervaux, S., and Gherardi, D.: JUICE navigation camera design, in: International Conference on Space Optics — ICSO 2018, edited by Karafolas, N., Sodnik, Z., and Cugny, B., p. 166, SPIE, https://doi.org/10.1117/12.2536086, 2019.

Grasset, O., Dougherty, M., Coustenis, A., Bunce, E., Erd, C., Titov, D., Blanc, M., Coates, A., Drossart, P., Fletcher, L., Hussmann, H., Jaumann, R., Krupp, N., Lebreton, J.-P., Prieto-Ballesteros, O., Tortora, P., Tosi, F., and Van Hoolst, T.: JUpiter ICy moons Explorer (JUICE): An ESA mission to orbit Ganymede and to characterise the Jupiter system, Planetary and Space Science, 78, 1–21, https://doi.org/10.1016/j.pss.2012.12.002, 2013.

Guerlet, S., Armante, R., Lauzanne, N., Poulet, F., Langevin, Y., Rodriguez, S., Fletcher, L., Fouchet, T., Piccioni, G., and Migliorini, A.: MAJIS performances in the infrared during the JUICE 2024 Earth fly-by: comparisons with IASI measurements and sensitivity to trace species, Annales Geophysicae, https://doi.org/10.5194/egusphere-2026-805, 2026.

Haffoud, P., Poulet, F., Vincendon, M., Filacchione, G., Barbis, A., Guiot, P., Lecomte, B., Langevin, Y., Piccioni, G., Dumesnil, C., Rodriguez, S., Carter, J., Stefania, S., Tommasi, L., Tosi, F., and Pilorget, C.: Calibration of MAJIS (Moons And Jupiter Imaging Spectrometer). III. Spectral calibration, Review of Scientific Instruments, 95, https://doi.org/10.1063/5.0188944, 2024.

Harris, C. R., Millman, K. J., van der Walt, S. J., Gommers, R., Virtanen, P., Cournapeau, D., Wieser, E., Taylor, J., Berg, S., Smith, N. J., Kern, R., Picus, M., Hoyer, S., van Kerkwijk, M. H., Brett, M., Haldane, A., del Río, J. F., Wiebe, M., Peterson, P., Gérard-Marchant, P., Sheppard, K., Reddy, T., Weckesser, W., Abbasi, H., Gohlke, C., and Oliphant, T. E.: Array programming with NumPy, Nature, 585, 357–362, https://doi.org/10.1038/s41586-020-2649-2, 2020.

Hueso, R., Antuñano, A., Lara, L. M., Stephan, K., Zinzi, A., Coustenis, A., Yair, Y., Sato, M., Haruyama, J., Simon, A., Tubiana, C., Penasa, L., Agostini, L., Luchetti, A., Aboudan, A., Aye, M., Kersten, E., Matz, K.-D., Politti, R., Trauthan, F., Evill, R., Belgacem, I., Yukihiro, T., Castro-Marín, J. M., Della Corte, V., Hviid, S., Roatsch, T., Schmitz, N., Patel, M., Portyankina, G., and Palumbo, P.: JUICE-JANUS observations of Earth in preparation for the JANUS investigation of Jupiter's atmosphere, Annales Geophysicae, https://doi.org/10.5194/egusphere-2026-710, 2026.

Hunter, J. D.: Matplotlib: A 2D Graphics Environment, Computing in Science &amp; Engineering, 9, 90–95, https://doi.org/10.1109/mcse.2007.55, 2007.

JMA/MSC: JMA Himawari-8/9, https://registry.opendata.aws/noaa-himawari/, 2021.

Langevin, Y., Carlier, V., Hannou, C., Gonnod, L., Carter, J., Tosi, F., Filacchione, G., Dumesnil, C., Piccioni, G., and Poulet, F.: H1RG readout procedures for MAJIS, the VIS/NIR imaging spectrometer of JUICE: impact on the performances, in: Space Telescopes and Instrumentation 2022: Optical, Infrared, and Millimeter Wave, edited by Coyle, L. E., Perrin, M. D., and Matsuura, S., p. 163, SPIE, https://doi.org/10.1117/12.2629310, 2022.

Langevin, Y., Poulet, F., Piccioni, G., Filacchione, G., Dumesnil, C., Tosi, F., Carter, J., Barbis, A., Haffoud, P., Tommasi, L., Vincendon, M., De Angelis, S., Guerri, I., Pilorget, C., Rodriguez, S., Stefani, S., Bolsée, D., Cisneros, M., Van Laeken, L., Pereira, N., and Carapelle, A.: Calibration of MAJIS (Moons and Jupiter Imaging Spectrometer). IV. Radiometric calibration (invited), Review of Scientific Instruments, 95, https://doi.org/10.1063/5.0202702, 2024.

Langevin, Y., Rodriguez, S., Guerlet, S., Poulet, F., Piccioni, G., Agostini, L., Armante, R., D'Aversa, E., Filacchione, G., Fletcher, L., Oliva, F., Royer, C., Seignovert, B., Stephan, K., Tosi, F., and Trent, T.: Post launch spectral and radiometric performances of MAJIS, the VIS-NIR imaging spectrometer of JUICE, Annales Geophysicae, https://doi.org/10.5194/egusphere-2026-410, 2026.

LOLA Science Team and Goddard Space Flight Center: Moon LRO LOLA DEM 118m, https://astrogeology.usgs.gov/search/map/moon_lro_lola_dem_118m, 2014.

LROC Team and Arizona State University: Moon LRO LROC WAC Global Morphology Mosaic 100m, https://astrogeology.usgs.gov/search/map/moon_lro_lroc_wac_global_morphology_mosaic_100m, 2013.

Lucchetti et al.: Morphological and Spectrophotometric exploitation of JANUS LEGA Dataset: Langrenus impact crater characterization and evolution of the highland “isthmus” between Mare Fecunditatis and Mare Tranquillitatis, Annales Geophysicae, 2026.

Martin Raspaud, David Hoese, Panu Lahtinen, Gerrit Holl, Simon Proud, Stephan Finkensieper, Andrea Meraner, Adam Dybbroe, Panu Lahtinen, Johan Strandgren, yukaribbba, Joleen Feltz, BENR0, Sauli Joro, Xin Zhang, Pierre de Buyl, Youva, Gionata Ghiggi, William Roberts, Lars Ørum Rasmussen, ClementLaplace, Olivier Samain, mherbertson, Jorge Humberto Bravo Méndez, Yufei Zhu, Isotr0py, seenno, rdaruwala, and bkremmli: pytroll/satpy: Version 0.60.0 (2026/03/04), https://doi.org/10.5281/ZENODO.596324, 2026.

Met Office: Cartopy: a cartographic Python library with a Matplotlib interface, Exeter, Devon, https://cartopy.readthedocs.io, 2010 - 2015.

NOAA: Geostationary Operational Environmental Satellites (GOES) 16, 17, 18 & 19, https://registry.opendata.aws/noaa-goes/, 2022.

Oliva, F., D’Aversa, E., Migliorini, A., Piccioni, G., Poulet, F., Langevin, Y., Filacchione, G., Ciarniello, M., Rodriguez, S., Seignovert, B., Mura, A., Fletcher, L. N., Zinzi, A., Giardino, M., Lopinto, E., Sindoni, G., and Plainaki, C.: JUICE-MAJIS Earth observations during the 2024 gravity assist: first analysis and comparison with PRISMA data, Annales Geophysicae, https://doi.org/10.5194/egusphere-2025-6455, 2026.

Palumbo, P., Roatsch, T., Lara, L. M., Castro-Marin, J. M., Della Corte, V., Hviid, S., Jaumann, R., Michaelis, H., Patel, M. R., Portyankina, G., Schmitz, N., Amoroso, M., Mugnuolo, R., Aboudan, A., Agostini, L., Althaus, C., Álvarez, F., Bartolomei, M., Behnke, T., Bilotta, T., Colombatti, G., Colosimo, A., Coustenis, A., Cremonese, G., Crews, C., Dattolo, A., Debei, S., Denk, T., Fiethe, B., Herranz, M., Hoffmann, H., Hueso, R., Koncz, A., Jiménez-Ortega, J., Lichopoj, A., Livi, L., Llamas, X., Lopes, R., Lucchetti, A., Martinez-Navajas, I., Mazzotta Epifani, E., Mertens, V., Pajola, M., Sarti, F., Schroedter, R., Stephan, K., Tosi, F., Tubiana, C., Wendler, B., Wendler, D., Williams, D., Wolff, F., Zusi, M., Chiodini, S., Ficai Veltroni, I., Galeotti, A., García-Segura, A., Greggio, D., Holland, A. D., Kenkmann, T., Leese, M. R., Magrin, D., Michalik, H., Munari, M., Noci, G. E., Paolinetti, R., Schipani, P., Soman, M., Stefanov, K. D., Turella, A., Aharonson, O., Bell, J. F., Bertini, I., Coates, A. J., Di Achille, G., Grassi, D., Groussin, O., Gwinner, K., Haruyama, J., Hauber, E., Hiesinger, H., Langevin, Y., Lainey, V., Marchi, S., Marinangeli, L., Marzari, F., Massironi, M., Mitri, G., Mottola, S., Oberst, J., Postberg, F., Poulet, F., Preusker, F., Schmidt, J., Schneider, N. M., Simon, A., Takahashi, Y., Tirsch, D., Vincendon, M., Balme, M. R., Bettanini, C., Borin, P., Capria, M. T., Elgner, S., Esposito, F., Ferranti, L., Ferrari, S., Fornasier, S., Galluzzi, V., Giacomini, L., Guzzetta, L., Jones, G. H., Kersten, E., Ledeit, L., Martellato, E., Matz, K.-D., Mennella, V., Murray, C., Otto, K. A., Pelizzo, M. G., Penasa, L., Politi, R., Popa, C., Pozzobon, R., Prieto Ballesteros, O., Re, C., Rotundi, A., Sato, M., Schmedemann, N., Shoji, D., Simioni, E., Sindoni, G., Trauthan, F., and Yair, Y.: The JANUS (Jovis Amorum ac Natorum Undique Scrutator) VIS-NIR Multi-Band Imager for the JUICE Mission, Space Science Reviews, 221, https://doi.org/10.1007/s11214-025-01158-6, 2025.

Poulet, F., Langevin, Y., and Piccioni, G.: Calibration of the Moons And Jupiter Imaging Spectrometer (MAJIS): Introduction to the special collection and summary of the performances, Review of Scientific Instruments, 95, https://doi.org/10.1063/5.0209679, 2024a.

Poulet, F., Piccioni, G., Langevin, Y., Dumesnil, C., Tommasi, L., Carlier, V., Filacchione, G., Amoroso, M., Arondel, A., D’Aversa, E., Barbis, A., Bini, A., Bolsée, D., Bousquet, P., Caprini, C., Carter, J., Dubois, J.-P., Condamin, M., Couturier, S., Dassas, K., Dexet, M., Fletcher, L., Grassi, D., Guerri, I., Haffoud, P., Larigauderie, C., Le Du, M., Mugnuolo, R., Pilato, G., Rossi, M., Stefani, S., Tosi, F., Vincendon, M., Zambelli, M., Arnold, G., Bibring, J.-P., Biondi, D., Boccaccini, A., Brunetto, R., Carapelle, A., Cisneros González, M., Hannou, C., Karatekin, O., Le Cle’ch, J.-C., Leyrat, C., Migliorini, A., Nathues, A., Rodriguez, S., Saggin, B., Sanchez-Lavega, A., Schmitt, B., Seignovert, B., Sordini, R., Stephan, K., Tobie, G., Zambon, F., Adriani, A., Altieri, F., Bockelée, D., Capaccioni, F., De Angelis, S., De Sanctis, M.-C., Drossart, P., Fouchet, T., Gérard, J.-C., Grodent, D., Ignatiev, N., Irwin, P., Ligier, N., Manaud, N., Mangold, N., Mura, A., Pilorget, C., Quirico, E., Renotte, E., Strazzulla, G., Turrini, D., Vandaele, A.-C., Carli, C., Ciarniello, M., Guerlet, S., Lellouch, E., Mancarella, F., Morbidelli, A., Le Mouélic, S., Raponi, A., Sindoni, G., and Snels, M.: Moons and Jupiter Imaging Spectrometer (MAJIS) on Jupiter Icy Moons Explorer (JUICE), Space Science Reviews, 220, https://doi.org/10.1007/s11214-024-01057-2, 2024b.

Poulet, F., Piccioni, G., Langevin, Y., Dumesnil, C., Carlier, V., Seignovert, B., Dexet, M., Fletcher, L. N., Leyrat, C., Altieri, F., Carter, J., D'Aversa, E., De Sanctis, M., Grassi, D., Guerlet, S., Le Mouélic, S., Migliorini, A., Oliva, F., Royer, C., Rodriguez, S., Stephan, K., Tosi, F., Zambon, F., Adriani, A., Arnold, G., Bibring, J.-P., Bockelée, D., Brunetto, R., Capaccioni, F., Carli, C., Cavalié, T., Cisneros González, M., Ciarnello, M., De Angelis, S., Drossart, P., Filacchione, G., Fouchet, T., Gérard, J.-C., Grodent, D., Irwin, P., Jacquinod, S., Karatekin, O., Lellouch, E., Ligier, N., Mangold, N., Mebsout, M., Merlin, F., Morbidelli, A., Mura, A., Nathues, A., Palumbo, M. E., Pilorget, C., Poch, O., Quirico, E., Raponi, A., Robert, S., Roussos, E., Sanchez-Lavega, A., Schmitt, B., Sindoni, G., Snels, M., Sordini, R., Stefani, S., Strazzulla, G., Trent, T., Tobie, G., Turrini, D., Vandaele, A.-C., Vincendon, M., Witasse, O., Vallat, C., and Moraino, A.: ESA/JUICE encounters Earth/Moon in 2024: overview of the Moons And Jupiter Imaging Spectrometer (MAJIS) observations, Annales Geophysicae, 44, 163–193, https://doi.org/10.5194/angeo-44-163-2026, 2026.

PSA: PSA Juice Majis Calibrated Dataset, https://doi.org/10.5270/esa-dhse3m2, 2029a.

PSA: PSA Juice Majis RAW Dataset, https://doi.org/10.5270/esa-8vbqca6, 2029b.

Rodriguez, S., Vincendon, M., Haffoud, P., Langevin, Y., Poulet, F., Quirico, E., Pilorget, C., Filacchione, G., Carter, J., Brunetto, R., Lecomte, B., Guiot, P., Dumesnil, C., and Piccioni, G.: Calibration of MAJIS (Moons and Jupiter Imaging Spectrometer): V. Validation with mineral samples and reference materials, Review of Scientific Instruments, 95, https://doi.org/10.1063/5.0215249, 2024.

Royer, C., Haffoud, P., Langevin, Y., Poulet, F., Bockelée-Morvan, D., D'Aversa, E., Cisneros-González, M., Grassi, D., Ligier, N., Piccioni, G., Carter, J., Tosi, F., Vincendon, M., Zambon, F., Zakharov, V., Gilles, M., and Seignovert, B.: A simulator of the MAJIS instrument onboard the JUICE mission: Description and application to operational and scientific cases, Planetary and Space Science, 264, 106 147, https://doi.org/https://doi.org/10.1016/j.pss.2025.106147, 2025.

Seignovert, Benoît Tobie, G., Robidel, R., Altobelli, N., Belgacem, I., Costa-Sitja, M., Vallat, C., Penasa, L., and Besch, Nathan amd D'Amore, M.: Planetary-coverage - Release 1.2.1, https://doi.org/10.60487/ZJFQ-H2C6, 2025.

Stefani, S., Piccioni, G., Poulet, F., Filacchione, G., Vincendon, M., Barbis, A., Tommasi, L., Guerri, I., Langevin, Y., Dumesnil, C., Haffoud, P., Rodriguez, S., Carter, J., Biondi, D., Boccaccini, A., De Angelis, S., Tosi, F., Pilorget, C., Guiot, P., and Lecomte, B.: Calibration of MAJIS (Moons and Jupiter Imaging Spectrometer): VI. The inflight calibration unit (ICU) (invited), Review of Scientific Instruments, 96, https://doi.org/10.1063/5.0221810, 2025.

Tosi, F., Royer, C., Colaiuta, F., Poulet, F., Powell, T. M., Greenhagen, B. T., Langevin, Y., Mura, A., Piccioni, G., Pilorget, C., Carli, C., and Zambon, F.: The JUICE 2024 close flyby of the Moon: Thermal assessment from MAJIS, Annales Geophysicae, https://doi.org/10.5194/egusphere-2025-6150, 2026.

Tubiana, C., Penasa, L., Agostini, L., Aboudan, A., Aye, M., Matz, K.-D., Read, M., Bilotta, T., Hueso, R., Lucchetti, A., Kersten, E., Politi, R., Portyankina, G., Seignovert, B., Trauthan, F., Zinzi, A., Evill, R., Dietz, A., Belgacem, I., Cornet, T., Castro-Marin, J. M., Della Corte, V., Hviid, S., Roatsch, T., Schmitz, N., Patel, M. R., Lara, L. M., and Palumbo, P.: Planning of the JUICE/JANUS camera observations during the first ever Lunar-Earth Gravity Assist, Annales Geophysicae, pp. 1–25, https://doi.org/10.5194/egusphere-2026-2008, 2026.

Vincendon, M., Guiot, P., Lecomte, B., Condamin, M., Poulet, F., Arondel, A., Barbay, J., Carter, J., De Angelis, S., Dumesnil, C., Filacchione, G., Haffoud, P., Hansotte, J., Langevin, Y., Mayeur, P.-L., Piccioni, G., Pilorget, C., Quirico, E., and Rodriguez, S.: Calibration of MAJIS (Moons And Jupiter Imaging Spectrometer). I. On-ground setup description and characterization, Review of Scientific Instruments, 95, https://doi.org/10.1063/5.0226567, 2024.

Virtanen, P., Gommers, R., Oliphant, T. E., Haberland, M., Reddy, T., Cournapeau, D., Burovski, E., Peterson, P., Weckesser, W., Bright, J., van der Walt, S. J., Brett, M., Wilson, J., Millman, K. J., Mayorov, N., Nelson, A. R. J., Jones, E., Kern, R., Larson, E., Carey, C. J., Polat, İ., Feng, Y., Moore, E. W., VanderPlas, J., Laxalde, D., Perktold, J., Cimrman, R., Henriksen, I., Quintero, E. A., Harris, C. R., Archibald, A. M., Ribeiro, A. H., Pedregosa, F., van Mulbregt, P., Vijaykumar, A., Bardelli, A. P., Rothberg, A., Hilboll, A., Kloeckner, A., Scopatz, A., Lee, A., Rokem, A., Woods, C. N., Fulton, C., Masson, C., Häggström, C., Fitzgerald, C., Nicholson, D. A., Hagen, D. R., Pasechnik, D. V., Olivetti, E., Martin, E., Wieser, E., Silva, F., Lenders, F., Wilhelm, F., Young, G., Price, G. A., Ingold, G.-L., Allen, G. E., Lee, G. R., Audren, H., Probst, I., Dietrich, J. P., Silterra, J., Webber, J. T., Slavič, J., Nothman, J., Buchner, J., Kulick, J., Schönberger, J. L., de Miranda Cardoso, J. V., Reimer, J., Harrington, J., Rodríguez, J. L. C., Nunez-Iglesias, J., Kuczynski, J., Tritz, K., Thoma, M., Newville, M., Kümmerer, M., Bolingbroke, M., Tartre, M., Pak, M., Smith, N. J., Nowaczyk, N., Shebanov, N., Pavlyk, O., Brodtkorb, P. A., Lee, P., McGibbon, R. T., Feldbauer, R., Lewis, S., Tygier, S., Sievert, S., Vigna, S., Peterson, S., More, S., Pudlik, T., Oshima, T., Pingel, T. J., Robitaille, T. P., Spura, T., Jones, T. R., Cera, T., Leslie, T., Zito, T., Krauss, T., Upadhyay, U., Halchenko, Y. O., and Vázquez-Baeza, Y.: SciPy 1.0: fundamental algorithms for scientific computing in Python, Nature Methods, 17, 261–272, https://doi.org/10.1038/s41592-019-0686-2, 2020.

Zambon, F., Altieri, F., De Sanctis, M. C., Le Mouélic, S., Piccioni, G., Poulet, F., Langevin, Y., Royer, C., Tosi, F., Karatekin, O., Mura, A., and Carli, C.: Spectral analyzes of lunar regions observed by MAJIS during the JUICE Earth-Moon flyby, Annales Geophysicae, https://doi.org/10.5194/egusphere-2026-876, 2026.